5-24-2010

Photoacoustic Reporter Gene Imaging And Optical Coherence Computed Tomography

Li Li
Washington University in St. Louis

Follow this and additional works at: https://openscholarship.wustl.edu/etd

WASHINGTON UNIVERSITY IN ST. LOUIS

School of Engineering and Applied Science

Department of Biomedical Engineering

Dissertation Examination Committee:

Prof. Lihong V. Wang, Chair

Prof. Younan Xia

Prof. Igor R. Efimov

Prof. Donald L. Elbert

Prof. Timothy P. Fleming

Prof. Lan Yang

PHOTOACOUSTIC REPORTER GENE IMAGING AND OPTICAL COHERENCE
COMPUTED TOMOGRAPHY

by

Li Li

A dissertation presented to the

Graduate School of Arts and Sciences of Washington University

in partial fulfillment of the requirements for the degree of

DOCTOR OF PHILOSOPHY

December 2010

St. Louis, Missouri

copyright by

Li Li

2010

Abstract of the Dissertation

Photoacoustic Reporter Gene Imaging and Optical Coherence Computed Tomography

by

Li Li

Doctor of Philosophy in Biomedical Engineering

Washington University in St. Louis, 2010

Research Advisor: Lihong V. Wang

Advances in imaging technologies have always been the major driving forces for the evolution of biomedical research. Compared with other modalities, optical imaging possesses several prominent merits. Because light interacts with tissue at the microscopic level through many distinct physical mechanisms, optical methods allow sensitive exploration of various aspects of the life down to the single-molecule level. From the technical perspective, optical systems utilize safe non-ionizing radiation, could be implemented at relatively low cost, also have the potential to be miniaturized for portable or endoscopic applications. As a result, optical imaging tools are playing an increasingly important role in both laboratorial research and clinical practice. Among them, photoacoustic imaging (PAI) and optical coherence tomography (OCT) are the two fastest growing branches. PAI measures the laser-induced acoustic wave, and produces high-resolution images of the optically absorbing features of tissue at multiple length-scales. OCT detects singly backscattered photons, and enables real-time high-resolution

in vivo biopsy of tissue up to an optical transport mean-free-path. My doctoral research is focused on developing three novel optical imaging techniques based on the spirits of PAI and OCT.

In the first part of this study, we established a new paradigm to visualize gene expression *in vivo* based on optical absorption. In the post-genomic era, we are now being challenged to develop novel molecular imaging methods to identify the functions of genes. PAI can detect specific molecules according to their characteristic absorption spectra, thus is a promising candidate for molecular imaging of gene expression. The full potential of photoacoustic molecular imaging still remains to be explored. For the first time, we demonstrated imaging gene expression by PAI in living mice and rats, using a chromogenic *lacZ*/X-gal reporter gene system. We demonstrated the expression of the *lacZ* reporter gene can be detected by PAI as deep as 5 cm inside tissue. In addition, we showcased that PAI could follow gene expression from the microscopic to the macroscopic level. This work represents one of the pioneering efforts to extend photoacoustic methods for molecular imaging.

In the second part of this study, we developed a novel multimodal microscope, called the integrated photoacoustic and optical coherence microscope (iPOM), which combines PAI and OCT in a single imaging platform. PAI is predominantly sensitive to optical absorption, while OCT exploits optical scattering. By combining their naturally complementary imaging contrasts, iPOM can provide comprehensive information about biological tissue. We designed and built a reflection-mode prototype of iPOM, which fuses optical-resolution photoacoustic microscopy with spectral-domain optical

coherence tomography. The potential applications of iPOM in studying cutaneous and ocular microcirculation, and tissue engineering were demonstrated.

Finally, we invented a new optical tomography, named optical coherence computed tomography (optical CCT), which overcomes several major limitations of OCT. OCT relies on singly backscattered photons to obtain high-resolution images. Its image quality degrades fast with the increase of the depth, because the multiply scattered photons quickly become dominant at a penetration larger than 500 μm. As a result, OCT can only effectively penetrate ~1 mm into highly scattering tissue like skin. In addition, OCT is mainly sensitive to optical scattering, which does not reflect the molecular content of tissue directly. Optical CCT measures both singly and multiply scattered photons using a low-coherence interferometer. We make use of both types of photons by adopting a model-based reconstruction algorithm. The light-tissue interaction model was established using the time-resolved Monte Carlo method. The optical properties of the tissue were reconstructed from measurements by solving the inverse radiative transport problem under the first Born approximation. As a result, optical CCT could image deeper than OCT, and provide extra molecule-specific contrasts, such as optical absorption. We designed and built the first optical CCT system. In experiments, absorbing inclusions of 100 μm diameter were imaged with consistent quality through a 2.6-mm-thick (equivalent to ~3 transport mean-free-paths) tissue-mimicking phantom.

Acknowledgments

I owe my deepest gratitude to my mentor, Prof. Lihong Wang. He introduced me to the field of biomedical optics, and guided me closely through my Ph.D. study. It is really a rewarding experience for me to receive my doctoral degree under his supervision.

I would like to thank Dr. Younan Xia, Dr. Igor R. Efimov, Dr. Donald L. Elbert, Dr. Timothy P. Fleming and Dr. Lan Yang for their valuable advice and their time serving on my dissertation committee.

I would also like to thank all the former and current members in the optical imaging laboratory for their experimental assistance, inspiring discussion and friendship. Special thanks go to Dr. Konstantin Maslov, Dr. Geng Ku, Dr. Minghua Xu, Dr. Roger Zemp, Dr. Meng-lin Li, Dr. Xinmai Yang, Dr. Changhui Li, Dr. Sri-Rajasekhar Kothapalli, Dr. Dakang Yao, Xiao Xu, Zijian Guo, Xin Cai and Chi Zhang.

I am also grateful to staff in the Biomedical Engineering department (Karen Teasdale, Marina Shipova, Amanda Moritz, and Glen Reitz), and for their help. A special thanks to Jim Ballard for proofreading my manuscripts.

Finally, I am truly blessed with the love from my parents, Ruisheng Li and Xiujuan Zhu, and my dear wife, Wei Su. It is their sacrifice and support that always motivates me through my Ph.D. research. They deserve far more credit than that I can ever give them.

Dedicated to my parents and my wife.

Table of Contents

List of Tables

List of Figures

xiii

Abbreviations

^{18}F-FDG   2-deoxy-2-(^{18}F)fluoro-D-glucose

AR-PAM   Acoustic-resolution photoacoustic microscopy

BLI   Bioluminescence imaging

CCT   Coherence computed tomography

DOT   Diffuse optical tomography

FLI   Fluorescence imaging

Fluc   Firefly luciferase (reporter gene)

GFP   Green fluorescence protein (reporter gene)

Hb   Deoxy-hemoglobin

HbO$_2$ Oxy-hemoglobin

HSV1-tk   Herpes simplex virus type 1 thymidine kinase (reporter gene)

iPOM   Integrated photoacoustic and optical coherence microscopy

MAP   Maximum amplitude projection

MRI   Magnetic resonance imaging

NA   Numeric aperture

NIS   Sodium/iodine symporter (reporter gene)

OR-PAM   Optical-resolution photoacoustic microscopy

PACT	Photoacoustic computed tomography
PAM	Photoacoustic microscopy
PAI	Photoacoustic imaging
PET	Positron emission tomography
RTE	Radiative transfer equation
TfR	Transferrin receptor (reporter gene)
X-gal	5-bromo-4-chloro-3-indolyl-β-D-galactoside

Chapter 1   Introduction

Ever since Roentgen's discovery of X-ray in 1895, innovations in imaging technologies have always been important driving forces for the modernization of biology and medicine. However, current mainstream imaging modalities, such as X-ray computed tomography (CT), ultrasonography and magnetic resonance imaging (MRI), are still limited, especially in early detection of diseases and revealing molecule-specific information of biology. Hence, demanding biomedical applications keep pushing for new imaging techniques to offer new insights into the life. Recently, biomedical optical imaging is emerging as a promising candidate for meeting these challenges. Compared with other modalities, optical imaging possesses several prominent advantages in 1) providing a rich set of sensitive imaging contrasts, such as absorption, scattering, fluorescence and polarization, most of which are molecule-specific, 2) the utilization of safe non-ionizing radiation, 3) the potential to be miniaturized for portable or endoscopic applications, and d) the relatively low cost.

In soft tissue, the collective migration behavior of photons can be loosely classified into three regimes [1]. Within the first millimeter in tissue, a large portion of photons follow their incident directions and travel roughly along a ballistic trajectory. It is called the ballistic regime. Between 1 mm and 1 cm is the quasi-diffusive regime, where most photons have been scattered more than ten times and retain only a weak memory of their original directions. After 1 cm, photons virtually forget their incident angles, propagate

along randomized directions, and enter the diffusive regime. Optical imaging tools working in all the three regimes have been developed based on different strategies for diverse biomedical applications from the microscopic to the macroscopic level. Figure 1.1 summarizes major optical imaging techniques on a maximal penetration depth-to-spatial resolution graph. The blue diagonal in the plot indicates where the depth-to-resolution ratio is 100. Techniques located on and below this line are considered to be high-resolution, which means they could produce images with more than 100 effective pixels along each dimension. For microscopic applications, various high-resolution ballistic optical microscopes, such as confocal microscopy [2], multiphoton microscopy [3] and coherent anti-Stokes Raman scattering microscopy [4], can penetrate a few hundred microns into tissue, and see details of cells or sub-cellular organelles with diffraction-limited spatial resolution at the order of a fraction of a micron. Recently, a group of fluorescence nanoscopes [5], such as stimulated emission depletion microscopy [6], photoactivated localization microscopy [7], and stochastic optical reconstruction microscopy [8], pushed the envelope of spatial resolution even further and broke the optical diffraction resolution limit. These techniques utilize the switching between the bright and dark state of a fluorescence marker to record sub-wavelength features sequentially in time. They currently can penetrate a monolayer of living cells, and resolve down to ~20 nm. Looking into the future, the optical nanoscopy carries the hope to see individual molecules in living cells. In the macroscopic world, low-resolution diffuse optical tomography (DOT) [9] maps the optical properties of tissue by inversing measurements of diffusive photons. Although it could penetrate ~5 cm into tissue, the resolution is only ~1/5 of the tissue thickness. Nevertheless, DOT is sensitive to changes

in tissue's optical properties caused by physiological functions. It is being tested for clinical applications to detect early-stage breast cancer, evaluate individual treatment outcome of tumor therapy, and study brain functions, usually as a complementary method to another high-resolution imaging technique (for example, MRI).
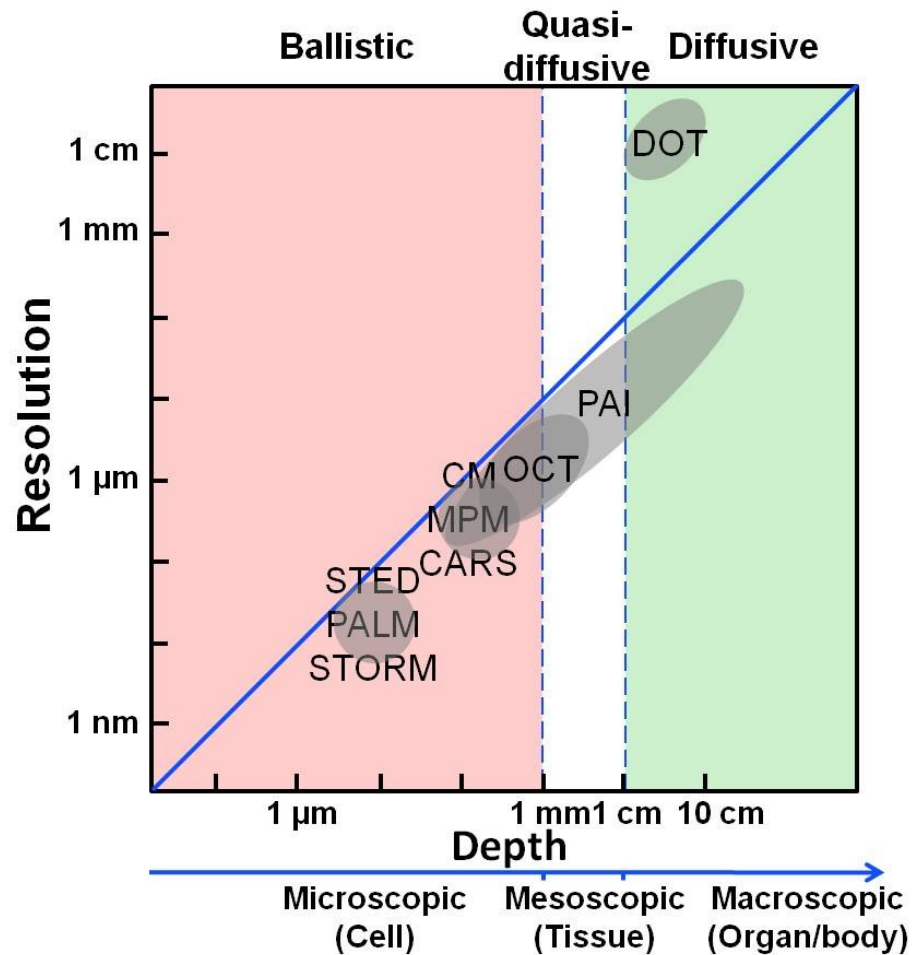
Figure 1.1 Survey of major biomedical optical imaging techniques. STED: stimulated emission depletion microscopy. PALM: photoactivated localization microscopy. STORM: stochastic optical reconstruction microscopy. CM: confocal microscopy. MPM: multiphoton microscopy. CARS: coherent anti-Stokes Raman scattering microscopy. OCT: optical coherence tomography. PAI: photoacoustic microscopy. DOT: diffuse optical tomography.

Recently, high-resolution photoacoustic imaging (PAI) and optical coherence tomography (OCT) are making increasing impact on both biomedical research and clinical diagnosis. They bridge the gap between the aforementioned microscopic and macroscopic optical imaging methods and are the two fastest growing branches in the field of biomedical optical imaging.

<u>Photoacoustic Imaging</u> As a physical phenomenon, the photoacoustic effect was first documented in 1880 by A. G. Bell, who invented the world's first wireless communication system – "Photophone" based on this discovery [10]. The photoacoustic effect describes a mechanism to listen to light-tissue interaction. When an object is irradiated by electromagnetic wave, part of the energy will be absorbed and further converted to heat. When the excitation is fast time-variant in energy, a transient increase in pressure will be induced through thermal-elastic expansion, and distributes spatially according to the object's optical absorbing structure. Finally, the initial pressure rise will propagate as an acoustic wave, named the photoacoustic wave, which could be detected outside the object. Assuming heat doesn't diffuse significantly during the short duration of excitation, the generation and propagation of the photoacoustic wave will be governed by the following general photoacoustic equation

$$\left(\nabla^2 - \frac{1}{v_s^2} \frac{\partial^2}{\partial t^2} \right) p = -\frac{\Gamma}{v_s^2} \frac{\partial(\eta_{th} \mu_a \Phi)}{\partial t} \tag{1.1}$$

,

4

which links the measured photoacoustic pressure p to the distribution of the optical absorption coefficient μ_a in the object. Here, v_s denotes the speed of sound. Γ is the Grueneisen parameter, a constant connecting thermal energy and mechanic energy in material. η_{th} is the percentage of absorbed electromagnetic energy that is converted to heat. Φ is the local optical fluence rate.

Photoacoustic imaging (PAI) refers to a novel imaging modality to visualize the absorbing features of tissue based on the photoacoustic effects. With the advent of laser, ultrasonic transducer, and imaging sciences, PAI has emerged rapidly as a new tool for both laboratorial investigation and clinical diagnosis since 2003 (See reviews [11-16]). By combining the merits of optical absorption contrast and ultrasonic detection, PAI possesses the following key advantages:

1) PAI is the only available imaging technique, which has 100% relative sensitivity to the molecule-specific optical absorption contrast. Optical absorption is a quantitative measure of the molecular content of tissue. A small fractional variation in the optical absorption coefficient in objects causes the same percentage of change in the measured photoacoustic signal. As a result, PAI can be used to quantitatively assess molecular-specific events. Many intrinsic physiologically important molecules, such as hemoglobin, melanin, and water, strongly absorb light in the visible and near-infrared parts of the optical spectrum. As a result, using endogenous contrast, PAI can visualize blood vasculature [17-19], melanin-containing lesions [20], and potentially edema [21]. In addition, the local concentration of a specific molecule could be quantified by measuring the photoacoustic signal at multiple optical wavelengths and

5

then solving a group of linear equations. For example, estimation of the local concentrations of the two different forms of hemoglobin, oxy-hemoglobin (HbO_2) and deoxy-hemoglobin (Hb), in single blood vessel has been demonstrated. As a result, PAI can quantify two key functional indicators of the local metabolism, the local total hemoglobin concentration (THb), and the blood oxygen saturation level (SO_2) [22]. What's more, PAI can be applied to study molecular biology by introducing exogenous contrast agents that modulate optical absorption, such as a chromogenic reporter gene assay [23, 24], organic dye [25] or nanoparticles [26].

2) PAI is capable of imaging with high resolution at all the three regimes of photon migration, and could become an important link between biomedical research in the microscopic level and the macroscopic level. An unparalleled advantage of PAI is that it, when implemented in different ways, can provide scalable imaging depth and spatial resolution suitable for multi-scale studies in from cells to humans. In the microscopic level, optical-resolution photoacoustic microscopy (OR-PAM) [19, 27, 28] was proposed to confine photoacoustic excitation inside a tight optical focus, and achieves an optical diffraction-limited lateral resolution down to a fraction of a micron. With an optical focusing of numeric aperture (NA) = 0.1, OR-PAM is capable of quantifying hemodynamic functions in each single blood micro-vessel and is good at characterizing microcirculation [29]. Most recently, our group has demonstrated OR-PAM could resolve individual red blood cells in single capillaries [27], and sub-cellular organelles in melanoma cells [28]. In the quasi-diffusive regime (1mm ~ 1cm in tissue), optical focusing works poorly. Acoustic-resolution photoacoustic microscopy (AR-PAM) was developed to detect the photoacoustic

6

www.manaraa.com

signal using a high-frequency focused ultrasonic transducer [18, 30, 31]. Because sound scatters 2 ~ 3 orders of magnitude less than light in tissue, AR-PAM could maintain a relatively good spatial resolution (tens of microns) beyond the penetration of other high-resolution optical imaging modalities (~1 mm). Till now, AR-PAM has been applied to diagnose subcutaneous melanoma [20], and monitor brain functions in small animals [32]. In the macroscopic world, photoacoustic computed tomography (PACT) [17] is able to penetrate beyond 5 cm into biological tissue [33] while maintaining sub-mm spatial resolution. In PACT, deeply seated absorbers are excited by diffusive photons. The generated photoacoustic signal is measured at different locations surrounding the object by a low-frequency scanning single-element transducer or an ultrasonic array. A reconstruction algorithm is applied to inverse the measurements to form an image. Due to its deep penetration, PACT is mostly targeted at clinical applications, such as screening breast cancer [34], imaging neonate brains [35], and mapping the sentinel lymph nodes [36], etc.

3) PAI produces images devoid of speckle artifacts. (See Appendix A for details.) Other coherent imaging techniques (such as ultrasonography, OCT, etc.) suffer from strong speckle artifact, a randomized granular mask obscuring images. Speckles deteriorate the image quality significantly by reducing both the effective spatial resolution and the detectability of small lesions. By contrast, PAI possesses an intrinsic mechanism to suppress speckles. We found this unique advantage of PAI is again due to its dependence on the optical absorption contrast [27]. All optical absorbers expand on laser excitation, and therefore all initial photoacoustic pressure rises are positive, which engenders strong correlations among the photoacoustic waves from the

7

absorbers. As a result, prominent boundaries always build up in photoacoustic images and suppress the interior speckle.

Optical coherence tomography   First proposed in 1991 [37], optical coherence tomography (OCT) works mostly in the ballistic regime. It allows real-time *in vivo* biopsy of tissue with μm-scale spatial resolution up to ~1 mm deep inside highly scattering tissue like skin. OCT is currently the most successful paradigm of clinical translation of optical imaging modality. According to a recently released market research report, the current global OCT market is around $200 million/year and grows at an annual rate of 34%. This rapid growth is expected to continue for the next several years, and the revenue will exceed $800 million by 2012 [38]. OCT is now a routine clinical examining tool in ophthalmology [39-44]. Eyes are relatively transparent to light, and ophthalmological OCT can penetrate through the eyes and diagnoses diseases in both retina and the anterior segment. Recently, the use of OCT through a catheter provides access to internal organs and has further broadened its applications to cardiology [45, 46] and gastroenterology [47-49]. Also, other applications of OCT in dermatology [50, 51], neurology [52, 53], dentistry [54, 55], and developmental biology [56, 57], are also under intensive investigation.

From the technical perspective, OCT is an optical analog to B-mode ultrasonography, except that it uses low-coherence light instead of a short ultrasonic pulse for depth ranging. An OCT system is basically an optical interferometer, which mixes the backscattered light from tissue with a reference light reflected by a mirror. The

8

interference between the two is recorded by a square-law detector. Thanks to the adoption of low-coherence light sources, photons backscattered from different depth could be separated with a superior axial resolution according to the coherence length of the source (typically 1 ~ 20 µm). Another advantage of OCT is that it can exploit the Doppler principle to measure blood flow *in vivo* [58-62]. Doppler OCT can estimate depth-resolved blow flow as slow as 10 µm/s with micrometer-scale spatial resolution. Comparing with widely used Doppler ultrasound, it provides ~2 orders better velocity sensitivity and more than 1 order better spatial resolution.
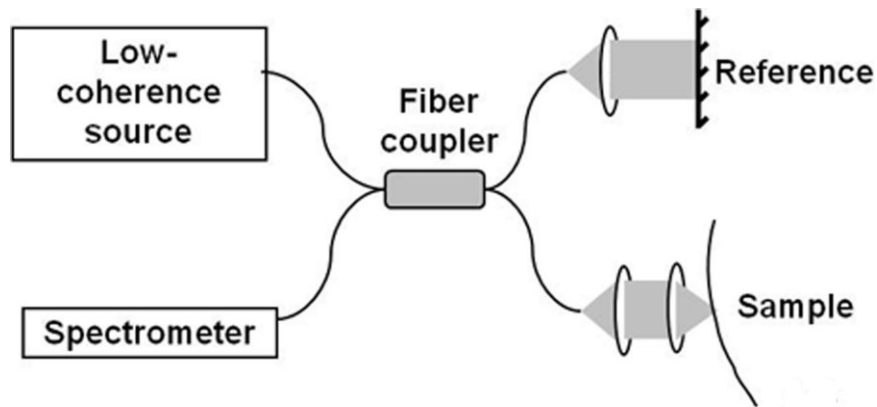
Figure 1.2   Schematic of a fiber-based spectral-domain implementation of optical coherence tomography.

Figure 1.2 shows a simplified schematic of a typical spectral-domain implementation of OCT, which is the foundation of my research elaborated in Chapters 3&4. The interference signal here is recorded as a spectrum using a high-resolution spectrometer, which can be written as

9

$$I(k) = S(k)\{r_R^2 + \left|\int_{-\infty}^{\infty} r_s'(z)\cos(2kn_s z)dz\right|^2 + r_R\int_{-\infty}^{\infty} r_s'(z)\cos(2kn_s z)dz\}, \qquad (1.2)$$

where $S(k)$ is the power spectrum of the low-coherence source as a function of wavenumber k. r_R denotes the amplitude reflectivity of the mirror in the reference arm, while $r_s'(z)$ is the amplitude reflectivity density of the sample at depth z. n_s is the refractive index of sample. In Equation (1.2), the first and the second terms are the power spectra of the light reflected back from the reference mirror and backscattered light from the tissue, respectively. Both of them are removed using calibration procedures. The third term codes the image, and represents the cross-interference between light from reference and sample. This scattering profile of tissue can be obtained from it through an inverse Fourier transform as

$$I(z) = \mathcal{F}^{-1}\{r_R S(k)\int_{-\infty}^{\infty} r_s'(z)\cos(2kn_s z)dz\} = \Omega(z) * \{r_s'(z) + r_s'(-z)\}, \qquad (1.3)$$

where $\Omega(z)$ is the autocorrelation function of light source, which determines the axial resolution of the system. In OCT, $r_s'(z)$ is presented as an image, and represents the depth-resolved reflectivity of tissue. We also noted that there exists a mirrored term $r_s'(-z)$, which is symmetrical to $r_s'(z)$ with respect to the point $z = 0$. By carefully setting the length of the reference arm, this mirrored image can be easily separated from the real image.

10

In my doctoral research, I developed three novel optical imaging techniques based on the spirits of PAI and OCT.

In Chapter 2, I summarized our work on establishing a new way to visualize the expression of a gene *in vivo* based on optical absorption using PAI [23, 24]. In the post-genomic era, we are being challenged to develop new molecular imaging methods to monitor the gene expression in living organisms and decipher the functions of genes. PAI can detect specific molecules according to their characteristic absorption spectra, thus is a promising candidate for molecular imaging. Here, for the first time, we proposed a new paradigm of molecular imaging to study gene expression *in vivo* using PAI and a chromogenic reporter gene system. We demonstrated imaging the expression of the *lacZ* reporter gene using PAI in living rats and mice, following the introduction of the sensitive colorimetric X-gal assay. We demonstrated the expression of *lacZ* can be detected by PAI as deep as 5 cm in biological tissue. In addition, we showcased that PAI could follow the gene expression from the microscopic level to the macroscopic level. This work represents one of the pioneering efforts to extend photoacoustic methods for molecular imaging.

In Chapter 3, I summarized our development of a novel multimodal microscope, named the integrated photoacoustic and optical coherence microscope (iPOM) [63]. iPOM combines PAI and OCT in a unified imaging platform. PAI is predominantly sensitive to optical absorption, while OCT exploits optical scattering. By combining their naturally complementary imaging contrasts, iPOM can provide comprehensive information about biological tissue. We designed and built a prototype of iPOM, and demonstrated its

11

potential applications in studying cutaneous and ocular microcirculation, and tissue engineering.

In Chapter 4, I summarized our invention of a new optical tomography, the optical coherence computed tomography (optical CCT). Optical CCT overcomes several major limitations of OCT. Traditionally, OCT assumes all detected photons are scattered only once in tissue. However, a photon will be scattered an average of 10 times after traveling 1 mm inside normal soft tissue. Multiply scattered photons blur the OCT image, and are generally considered as noise. Consequently, OCT suffers from fast degradation in imaging quality with the increase of depth, and can only penetrate ~1 mm when imaging highly scattering tissue like skin. What's more, OCT is mainly sensitive to optical scattering, and is limited in terms of providing molecule-specific information. Optical CCT measures both singly and multiply scattered photons by low-coherence interferometry, similar to OCT. However, optical CCT makes use of both types of photons using a model-based reconstruction. We established a light-tissue interaction model based on the time-resolved Monte Carlo method. The optical properties of the tissue were reconstructed from the measurements by solving the inverse transient radiative transport problem using this model under the first Born approximation. We designed and built the first optical CCT system. We proved that optical CCT could imaging deeper than OCT, and provide extra molecule-specific contrasts, such as optical absorption. In experiments, absorbing inclusions of 100 µm diameter were imaged with consistent quality through a 2.6-mm-thick (equivalent to ~30 scattering mean-free-paths) high-scattering tissue-mimicking phantom.

12

Finally, in Chapter 5, I summarized this work and suggested potential future directions.

In addition, in Appendix A, I included our work to theoretically understand the speckle-free nature of PAI, which was previously an unsolved puzzle to many researchers in this field.

13

Chapter 2   Photoacoustic Molecular Imaging of

Reporter Gene Expression *In Vivo*[*]

2.1   Motivation for Molecular Imaging of Gene Expression

The accomplishment of the human genome project in 2003 launched a new revolution in both biomedical research and clinical practice. For 13 years, scientists across the world deciphered the blueprint of the human life, and completed a high-quality sequence of the entire human genome that contains ~3.2 billion base pairs. Surprisingly, it was found that the enormous human genome only contains in 2% of its entire length a total of 20,000 ~ 25,000 genes, which encode all the proteins responsible for building human body and executing physiological functions [64].

In the post-genomic era, we are now being challenged to identify the functions of the discovered genes, understand the molecular mechanisms of physiology and pathology, and develop personalized treatment of diseases. [65] All these investigations require evaluating the expression patterns of genes. Traditionally, gene expression studies were carried out *in vitro* using cell lysates. Most methods, including northern blotting, reverse transcription quantitative polymerase chain reaction, DNA microarray, and serial analysis of gene expression, measure mRNA, the intermediate transcriptional product of genes, to

---

[*] Reprinted with permission from (1) L. Li, R. J. Zemp, G. Lungu, G. Stoica, and L. V. Wang, "Photoacoustic imaging of lacZ gene expression in vivo," Journal of Biomedical Optics 12, 020504 (2007) and (2) L. Li, H. F. Zhang, R. J. Zemp, and L. V. Wang,

14

infer the level of gene expression. Proteins, the final expression product of gene, can be assessed with western blotting [66]. There are several major limitations with these approaches. (a) Their results may not correspond to what happens *in vivo*, due to the complexity of replicating the native microenvironment. (b) They produce only a single data point from each cell culture or sacrificed animal. To overcome the intrinsic variation among individuals, or to get longitudinal information, procedures must be repeated on a large number of samples or animals to get statistically robust results. As a result, the traditional gene expression studies are labor-intensive, time-consuming, and extremely costly. (c) They are incapable of localizing where gene expression happens in cells. (d) The level of mRNA for a gene may not quantitatively correlate with the protein product of the same gene [67] due to the varied translational and post-translational regulation of gene expression.

With the promise of overcoming these limitations of the above *in vitro* tools, molecular imaging is rapidly emerging as a promising candidate for interrogating gene expression *in vivo* [68-70]. Conventional imaging methods reveal the anatomical and functional features inside bodies, and provide only non-specific information about the foundational molecular events. By contrast, molecular imaging marries start-of-art imaging technologies with modern molecular biology methodology to look at specific molecular events underlying physiology and pathology, and is viewed by many as the next generation of medical imaging. In a typical molecular imaging protocol, an exogenous "molecular probe" is introduced into the body, interacts specifically with intrinsic molecules of interest and gives out a localized physical signal that could be visualized by an imaging modality. As a result, molecular imaging can visualize the spatiotemporal

15

distribution of specific proteins, the ultimate products of gene expression, within their native environment *in vivo*. Thanks to the non-invasive nature of molecular imaging, animals studied serve as their own control in a longitudinal study to minimize the uncertainty caused by the inter-sample differences. Thus, molecular imaging is expected to greatly facilitate gene expression research, by significantly reducing the animal use, workload and financial investment. From the clinical perspective, molecular imaging could potentially reveal the causes of diseases besides the resultant symptoms, and represents a significant paradigm shift for medical imaging. It is believed that molecular imaging could not only accelerate laboratorial research in molecular biology, but also deeply impact clinical practices by contributing to early detection and fast staging of diseases, accurate evaluation of treatment outcome, and rational design of novel therapy.

The expression of a gene can be studied by molecular imaging either directly or indirectly. In the direct category, molecular probes interact directly with the native protein product of an endogenous gene, and gives out imaging signals where they are expressed. As a classical example, the expression of the *Glut-1* gene can be evaluated by positron emission tomography (PET) using a radiotracer derived from 2-deoxy-2-(^{18}F)fluoro-D-glucose (FDG) to diagnose and stage cancer [71]. *Glut-1* codes a glucose transporter on the surface of cells, and is found to be over-expressed in most tumors. A radiolabeled analogue of glucose, ^{18}F-FDG, can serve as a molecular probe to facilitate PET imaging of the expression of *Glut-1*. Following injection, ^{18}F-FDG is first shipped into the cells by Glut-1 transporter just as the native glucose, then phosphorylated by hexokinase, and finally gets trapped inside cells. After non-phosphorylated probes are washed out through circulation, we can use PET to detect the intracellular radioactive

molecular probes, and localize malignant cells that are characterized by their hyper-metabolism of glucose. However, the direct assessment of endogenous gene expression using molecular imaging is limited, due to the fact that proper direct molecular probes need to be designed specifically for each gene-coded protein. Establishment of a single molecular probe involves identifying the configuration of targeted proteins, selection from a huge library of chemicals, and validation of efficacy and safety in cell cultures, animals and finally humans. This process generally requires significant efforts, time and investment. A recent review estimated that specific molecular probes have been developed for <5% of molecular markers of cancer [72]. Thus, another group of molecular imaging is developed to visualize gene expression indirectly using reporter genes. [73] A reporter gene is a short segment of exogenous DNA, which is virally or non-virally incorporated into the host genome, and codes a special protein product that can be readily visualized by an imaging tool, usually with the assistance of the corresponding reporter probe. These methods are attractive, because they are versatile in applications. In contrast with the direct methods, only a few reporter gene systems are required to be established for an imaging modality to study the expression of any endogenous genes. By inserting a reporter gene into the same reading frame as an endogenous gene, the regulation of different genes of interest under normal and pathological states can be studied. Also, through introducing a reporter gene constitutively under the control of a ubiquitous promoter, we can monitor the trafficking of the marked cells. In addition, protein-protein interactions could be studied using a transcriptional activation scheme [74]. In a pioneering work, S. Gambhir's group demonstrated repetitively molecular imaging the regulation of endogenous albumin gene

17

by visualizing the expression of herpes simplex virus type 1 thymidine kinase (*HSV1-tk*) reporter gene under the control of the albumin promoter using PET. [75]

In this chapter, I summarized my work in establishing a new paradigm to image gene expression *in vivo* using a novel physical contrast - optical absorption. We demonstrated the first photoacoustic molecular imaging of gene expression using a chromogenic reporter gene [23, 24]. Our work represents one of the pioneering efforts to extend photoacoustic methods for molecular imaging. Technical merits of photoacoustic molecular imaging in imaging depth and multi-scale research are also demonstrated.

2.2   Advantages of Photoacoustic Molecular Imaging

Not all existing imaging modalities are suitable for molecular imaging. Till now, only a few imaging technologies have been successfully exploited to depict reporter gene expression *in vivo* (summarized in Table 2.1). Among them, nuclear imaging, mainly PET, is most mature and is now moving towards clinical applications [76]. PET detects the paired γ-photons generated during the annihilation between the positron emitted by a radioactive probe and a nearby electron. It can image through the entire human body, and is sensitive to trace amounts (~pM) of accumulated molecular probes [77]. The major pitfalls of PET include poor spatial resolution (~6 mm with clinical systems, ~2 mm with microPET [77]), requirement of the proximity of a cyclotron, utilization of radioactive materials, and incapability of simultaneously studying expressions of multiple genes. Magnetic resonance imaging (MRI) measures the different relaxation rates of unpaired dipoles induced by a high magnetic field under various physiochemical environments. It

18

gives excellent soft tissue contrasts, achieves superior sub-mm spatial resolution [78] and has no penetration limit for medical imaging. However, in terms of molecular imaging, MRI suffers from its inherent low sensitivity (~mM level [69]). Sensitive reporter genes for MRI are still being actively pursued. Two optical imaging tools, bioluminescence imaging (BLI) and fluorescence imaging (FLI), are currently prevalent for molecular biology investigations in preclinical research: They sense photons emitted from specific molecular probes following a chemical reaction or optical excitation. BLI can detect extremely low signal at the level of fM, due to its virtually null background *in vivo*. FLI has a typical sensitivity on the order of nM, because it fights against the background of autofluorescence [69]. Another prominent advantage of the two optical methods is their high throughput rate, which is not available with current PET and MRI. The limitations shared by the two include limited imaging depth (~1 cm [69]), lack of depth resolution and poor lateral resolving power. Although μm-order resolution is achievable within a thin preparation of tissue, deeper structures are poorly resolved *in vivo* due to the nature of optical diffusion.

Table 2.1 Comparison among different molecular imaging modalities

Imaging modalities	Spatial resolution	Depth	Sensitivity	Representative reporter gene systems (*Type*)
PET	Poor	Excellent	Good	*NIS* gene with [^{124}I]iodide (*Transporter*)
MRI	Excellent	Excellent	Poor	*TfR* gene with Tf-MION (*Receptor*)
BLI	Poor	Poor	Excellent	*Fluc* gene with D-luciferin (*Enzyme*)
FLI	Poor	Poor	Good	*eGFP* (*Fluorescence protein*)
PAI	Excellent	Good	Good	*lacZ* with X-Gal (*Enzyme*)

Here, we propose photoacoustic imaging (PAI) will be the next promising candidate for molecular imaging. By exploiting optical absorption contrast, PAI is capable of detecting specific molecules according to their characteristic optical spectra. Compared with other molecular imaging modalities summarized above, we predict that PAI features the following remarkable merits for studying gene expression:

1) PAI utilizes non-ionizing radiation, and can safely follow the temporal regulation of a gene in the same subject through an extended study. As a comparison, PET use radioactive material, which presents a health risk when repetitively used.

2) PAI is well suited for studying multi-scale biology, and can cover the complete spectrum of gene expression studies from fundamental research in cell cultures to clinical applications in human. PAI is scalable in terms of spatial resolution and

20

imaging depth. When implemented in different ways, PAI can either resolve sub-cellular structures within the first few hundreds of microns into tissue, or penetrates several centimeters while retains sub-mm resolution. All aspects of gene expression can be potentially investigated with PAI based on the same physical contrast. Hence, we expect that, using PAI, laboratorial discoveries on genetic functions and therapy could be translated to applications in animal and human through an accelerated path.

3) In its deep-penetration version, PAI could visualize the three-dimensional expression pattern of a gene with sub-mm spatial resolution up to 5 cm deep inside highly-scattering biological tissue. As a comparison, BLI and FLI penetrate much shallower, lack the depth resolution, and obtain only mm-order lateral resolution.

4) PAI is sensitive, and can potentially detect low level of gene expression. The sensitivity of a particular photoacoustic molecular imaging protocol depends on a number of different parameters, including the resolution and noise floor, the depth and dimension of the target, the absorption cross-section of the molecular probe and the wavelength and intensity of the photoacoustic excitation, etc. In literatures, it was reported PAI was able to sense as low as ~10 pM of golden nanoparticles [79] and ~100 nM of organic dye [23, 80]. Generally speaking, the sensitivity of PAI is lower than BLI, comparable to PET and FLI, and better than MRI.

5) PAI can assess anatomical and physiological changes associated with the regulation of a gene using endogenous contrast. By detecting extrinsic chromophores, PAI can depict the morphology of tissue and quantify many crucial functional parameters,

such as the local oxygen saturation level, the local total hemoglobin concentration, blood flow, and temperature, etc.

6) PAI can study the expression of multiple genes in parallel. Spectroscopic PAI can differentiate different molecular probes based on their distinct absorption spectra. Thus, PAI can follow the expression of multiple genes using different molecular probes simultaneously, and allow us to reveal the complex genetic network. As a comparison, PET relies on 511-keV γ-photons regardless of molecular probes, and is only able to study one gene at a time.

Although PAI develops fast since 2003 in terms of structural and functional imaging, the potential of PAI in molecular imaging still remains to be explored. Table 2.2 summarizes both direct and indirect photoacoustic molecular imaging methods with demonstration in living organisms in literatures. In 2007, we first reported *in vivo* photoacoustic molecular imaging of the expression of the *lacZ* reporter gene in living rats and mice [23], and suggested that photoacoustic imaging could complement other existing molecular imaging modalities in studying the functions of genes. Most of other studies published later focused on using bioconjugated organic dyes or nanoparticles to directly target over-expressed cancer biomarkers to enable photoacoustic detection of tumors [25, 26, 81, 82]. Most recently, photoacoustic detection of other reporter genes coding fluorescence proteins has been reported [83]. Due to their considerable fluorescence emission, fluorescence proteins generally have a low efficiency of photoacoustic generation. Also, they lack of intrinsic amplification of molecular signal. As a result, this strategy only

worked in relatively transparent model organisms, such as Drosophila melanogaster pupa and zebrafish.

Table 2.2 Existing photoacoustic molecular imaging methods

Indirect			
Reporter gene	**Applications**	**Year**	**References**
lacZ	Monitoring *lacZ*-tagged 9L gliosarcoma in rats and mice	2007, 2008	[23, 24]
Fluorescence proteins, *eGFP* and *mCherry*	Monitoring *eGFP* and *mCherry* marked cells in Drosophila melanogaster pupa and zebrafish	2009	[83]
Direct			
Molecular probes	**Biomarker**	**Year**	**References**
Organic dye, IRDye800-c(KRDF)	$\alpha_v\beta_3$ integrins in U87 glioblastoma	2008	[25]
Gold nanorods, AuNR785-HER2 and AuNR1000-EGFR	HER2 and EGFR receptors in OECM1 and Cal 27 squamous cell carcinoma	2008	[26]
Single-walled carbon nanotube, SWNT-RGD	$\alpha_v\beta_3$ integrins in a U87 glioblastoma	2008	[81]
Gold nanocages, [Nle^4,D-Phe^7]-α-MSH-AuNC	α-MSH receptor in melanoma	2010	[82]

23

2.3   Chromogenic Reporter Gene System

In established methods, the proteins expressed by reporter genes work with specifically engineered reporter probes or light and generate radioactive, paramagnetic or luminescent signal that can be imaged by nuclear imaging, MRI, BLI or FLI. Based on the type of the reporter proteins, there exist four different kinds of reporter genes, which encode receptors, transporters, enzymes or fluorescence proteins, respectively. Representative examples of different report genes are listed in Table 2.1. The transferrin receptor (*TfR*) reporter gene produces a specific membrane receptor to transferrin, an iron-carrying protein responsible for regulating cellular uptake of iron. After binding with an engineered superparamagnetic reporter probe, a conjugate of transferrin and monocrystalline iron oxide (Tf-MION), the receptor is internalized. Thus, cells over-expressing *TfR* can be detected with MRI by a decrease in T2 signal [84]. In contrast to receptor that usually binds with its ligand in a 1:1 ratio, a transporter can accumulate a large number of probes inside cells to sensitively detect gene expression. The sodium/iodine symporter (*NIS*) reporter gene codes a membrane transporter that ships iodine into cells. Radioactive [^{124}I]iodide enables PET to detect the expression of *NIS* at a low level. [85] In BLI, the firefly luciferase (*Fluc*) reporter gene expresses an enzyme, which can oxidize its substrate D-luciferin to give out light. [86] An enzyme can work on multiple probes, thus generate a strong signal even when the reporter gene is expressed at a low level. Fluorescence protein reporter gene is special due to the fact that they do not require supplying additional molecular probes. The 2008 Nobel prize in chemistry was

24

awarded to the work on the development of the most famous member of this family, the green fluorescence protein (GFP). When excited with light, GFP emits light at a red-shifted wavelength and can be visualized by FLI. [87]

As a new paradigm, we propose here to image the expression of a chromogenic reporter gene *in vivo*. Although developed earlier than their counterparts, the chromogenic reporter genes were previously neglected for molecular imaging, largely due to the lack of tools to visualize their expression inside living organisms. PAI fills this vacancy, and, in our opinions, will rejuvenate the development of new *in vivo* chromogenic reporter gene systems to solve the post-genomic challenges. In this study, we selected the *lacZ* gene, one of the most widely used chromogenic reporter genes, as a demonstration of the principle. Originated from *E. Coli*, *lacZ* encodes β-galactosidase, a bacterial enzyme responsible for metabolizing lactose into glucose and galactose. The expression of *lacZ* can be assayed by several chromogenic assays. Among them, we chose to use the sensitive 5-bromo-4-chloro-3-indolyl-β-D-galactoside (X-gal) as our molecular probe *in vivo*. X-gal is a colorless analogue of lactose, where the glucose fragment is replaced by an indole-derivative. β-galactosidase cleaves the glycosidic linkage in X-gal and yields galactose and an optical transparent indoxyl monomer, 5-bromo-4-chloro-3-hydroxyindole. Afterwards, two of the monomers are oxidized and form a stable insoluble blue product, 5,5'-dibromo-4,4'-dichloro-indigo [Figure 2.1(a)]. [88] Figure 2.1(b) shows the dramatic chromogenic process during 24 hours after adding 20 mg/ml X-gal solution to the native cell lysate of transgenic 9L gliosarcoma cells expressing the *lacZ* reporter gene. There are other colorimetric assays for β-galactosidase activity, such as o-nitrophenyl-β-D-galactoside (ONPG). However, the blue product from X-gal

25

absorbs at a longer wavelength than the chromophores produced by those alternative assays, and allows us to detect the expression of *lacZ* at a greater depth in tissue.
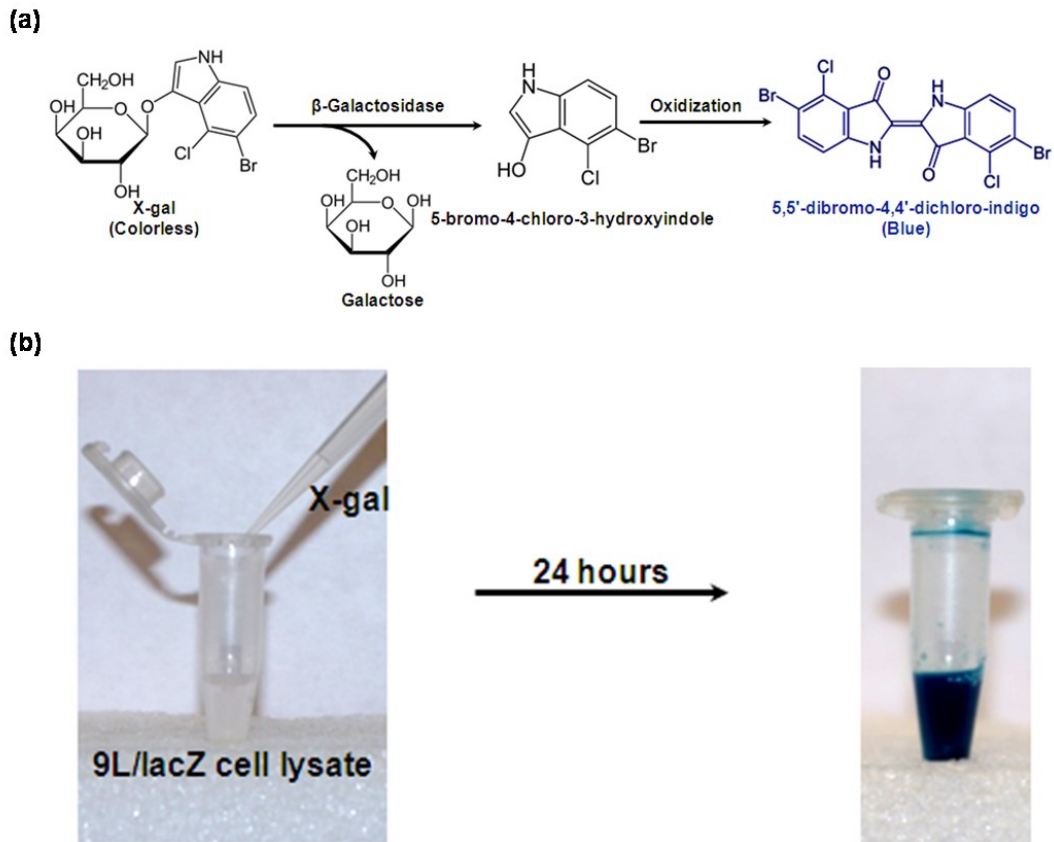
Figure 2.1 Detect the expression of the *lacZ* reporter gene using the chromogenic X-gal probe. (a) The hydrolysis of X-Gal catalyzed by β-galactosidase. (b) Photographs showing the chromogenic process by adding X-gal solution into the native lysate of 9L/*lacZ* cells.

For *in vivo* imaging, the *lacZ*/X-gal reporter gene system has two noticeable advantages. First, X-gal is an activatable probe. X-gal alone is colorless. Strong optical absorption is generated only after it is cleaved by β-galactosidase. Thus, the clearance of the un-cleaved X-gal before imaging is not required. As a result, the activity of β-galactosidase can be measured by PAI against a minimized background. Second, this enzymatic reporter system possesses an intrinsic signal-amplification mechanism. As an enzyme, a

26

single β-galactosidase molecule can cleave multiple X-gal molecules to produce a large number of blue product molecules, allowing us to detect a low expression level of *lacZ*.

Historically, the *lacZ*/X-gal reporter gene system has contributed extensively to genetic research as an indispensable *ex-vivo* technique. The blue-white screen built on this strategy is a standard tool for rapid selection of cells that are successfully transfected with the desired transgene. In addition, by assessing postmortem tissue samples, this reporter system has been used to investigate the coordinated gene expression in developmental biology [89], the regulation of specific promoters [90], the progression and metastasis of tumor [91, 92], and the outcome of gene therapy [93]. With PAI, all these researches could potentially be carried out *in vivo*.

Few other methods for *in vivo* imaging *lacZ* expression have been reported. One MRI approach used a β-galactosidase-cleavable paramagnetic molecular probe, which was introduced into an embryo of *Xenopus* at the two-cell stage [94]. Recently, FLI was used to image the fluorescent product from 9H-(1,3-dichloro-9,9-dimethylacridin-2-one-7-yl) β-D-galactopyranoside (DDAOG) cleaved by β-galactosidase [95]. PAI will complement these methods, and provide a new way to look at the expression of the *lacZ* gene at multiple length scales.

2.4 Quantitative Measurement of the Absolute Molar Extinction Coefficients of 5,5'-dibromo-4,4'-dichloro-indigo

The absorption spectrum of 5,5'-dibromo-4,4'-dichloro-indigo has not been documented previously to the best of our knowledge. In order to select the optimal parameters for photoacoustic imaging and quantify the expression of *lacZ*, we measured the absolute molar extinction coefficients of the blue product in the visible and near-infrared part of the optical spectrum. It is not a trivial task, because it is difficult to measure the concentration of the blue product.

In our experiment, we first obtained a total of 3.6 ml solution of natively expressed β-galactosidase by lysing the cultured 9L/*lacZ* cells. The cell lysate was divided equally into 5 cuvettes. 20 µl of X-gal solutions at concentrations of 2 mg/ml, 0.4 mg/ml, 0.2 mg/ml and 0.04 mg/ml were added to the cuvettes 1~4, while 20 µl of water was added to the last cuvette as the baseline [Figure 2.2(a)]. After given enough time for reaction, these solutions were measured for the optical absorbance from 500 nm to 900 nm using a commercial spectrometer (USB2000, Ocean Optics, Dunedin, FL). In order to compensate for the absorption spectrum of the solvent, the measured absorbance of the control solution was subtracted from those of solutions of blue products at each measured wavelength. Assuming all X-gal molecules were cleaved, we calculated the concentrations of the blue product according to the total amount of X-gal added. The assumption of enzyme excess was further confirmed by observing that the absorbance increases linearly with estimated concentration of the blue product at every single

wavelength [Figure 2.2(b)]. Finally, the absolute molar extinction coefficients of the blue product were obtained as the slope of the fitted lines in Figure 2.2(b).
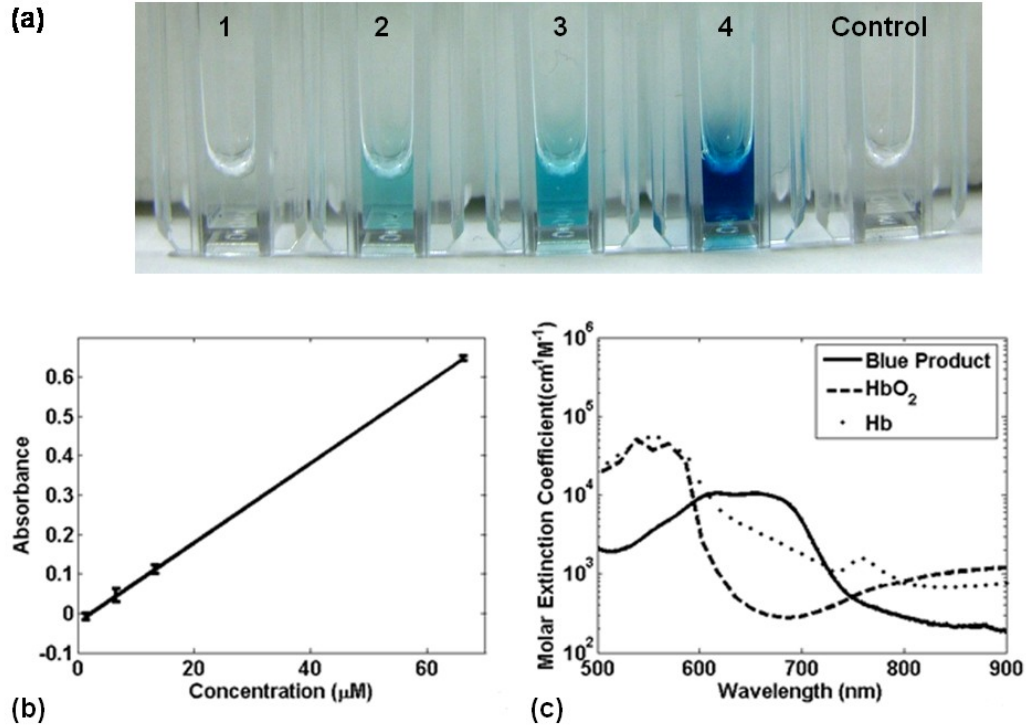
Figure 2.2   Measurement of the absolute molar extinction coefficients of the blue product, 5,5'-dibromo-4,4'-dichloro-indigo. (a) Cuvettes 1~4: 720 µl of cell lysate + 20 µl of X-gal solutions at 2 mg/ml, 0.4mg/ml, 0.2mg/ml and 0.04 mg/ml. The control cuvette: 720 µl of cell lysate + 20 µl of water. (b) Linear fitting of measured absorbance of solutions with varying concentrations of the blue product at 650nm. (c) Comparison among absorption spectra of the blue product, HbO_2 and Hb.

In Figure 2.2(c), we compared the measured molar extinction spectrum of the blue product with those of the main intrinsic absorbers: oxy-hemoglobin (HbO_2) and deoxy-hemoglobin (Hb). The absorption of the blue product peaks between 605 ~ 665 nm, which is part of the well the well-recognized "optical window" in biological tissue for optical imaging. Because endogenous chromophores of tissue (HbO_2 and Hb) absorb the

29

least within this spectral region, light can penetrate deeply into tissue and the expression of *lacZ* can be sensitively detected over a minimized background. For example, at 650 nm, the absolute molar extinction coefficient of the blue product was calculated to be 1.04×10^4 cm^{-1}M^{-1}, compared to 368 cm^{-1}M^{-1} of HbO$_2$ and 3.75×10^3 cm^{-1}M^{-1} of Hb. Assuming the background tissue had a averaged blood oxygenation of 75% and a normal tissue hemoglobin concentration of 30 mg/100 g [96], we estimated that, with single-wavelength excitation at 650 nm, PAI can detect as low as 523 nM of the blue product with a 1:1 contrast-to-background ratio.

2.5   Imaging the *lacZ* Expression *In Vivo* with Multi-scale PAI

We demonstrated photoacoustic molecular imaging of gene expression by visualizing transgenic 9L gliosarcoma, which constitutively expresses the *lacZ* reporter gene, implanted in living rats and mice by multiple PAI systems.

2.5.1   Circular-scanning Photoacoustic Computed Tomography

First, we show that an "invisible" tumor could be detected according to the *lacZ*/X-gal reporter gene system using a circular-scanning photoacoustic computed tomography.

Figure 2.3 shows the obtained photoacoustic images of subcutaneous 9L/*lacZ* tumor in Sprague Dawley rats before and after injection of X-gal. Before injecting X-gal, while the median fissure of the brain and some small cortical vessels were visible, the tumor was not [Figure 2.3(a)]. Following X-gal injection at points indicated by arrows in Figure 2.3(c), the tumor became prominent in Figure 2.3 (b). No signal up-regulation was

30

observed at the right-side injection point, which served as a negative control. Figure 2.3(c) is the photograph of the rat head following X-gal injection and just prior to imaging. Although a small bump is present, the exact shape of the tumor and distribution of *lacZ* expression was unknown. Figure 2.3(d) is the underside of the dissected scalp in the rectangular region indicated in Figure 2.3(c), showing the X-gal stained tumor, which is dark blue in color.
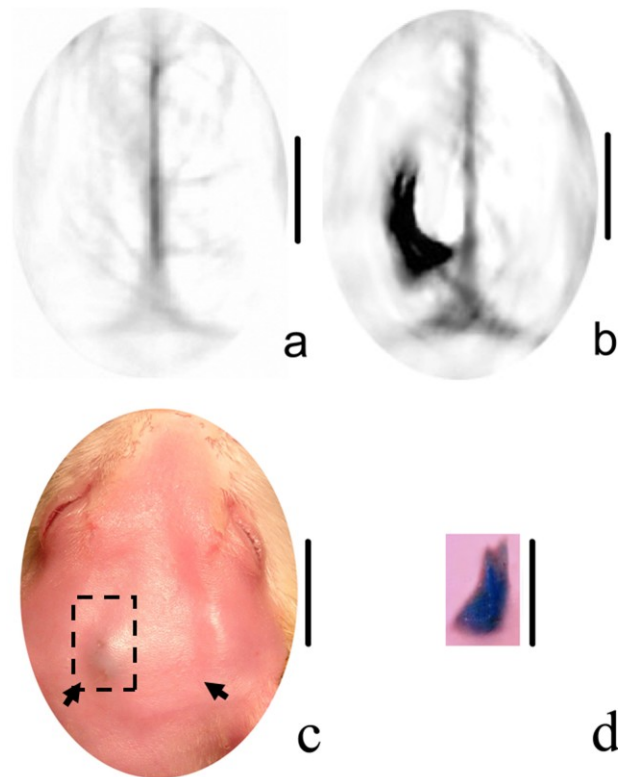
Figure 2.3   Detecting an "invisible" tumor by circular-scanning photoacoustic computed tomography using the *lacZ*/X-gal reporter gene system. (a) and (b) Photoacoustic images before and after the injection of X-gal. (c) Photograph of the rat's head after X-gal injection. The two arrows indicate the position of injection of X-gal. (d) Photograph of the underside of the rat's scalp in the rectangular region in (c), excised after sacrificing the animal. The scale bars represent 5mm.

To estimate the molar sensitivity, we imaged a tube (Inner diameter: 250 μm), transparent to light and ultrasound, filled with a solution of blue product at a concentration of 5.4

31

μM and embedded 5 mm deep in chicken breast tissue. The region with blue product was imaged with a contrast-to-background ratio (CBR) of 10.5. Hence, the minimum detectable concentration of blue product (with CBR=1) was less than 515 nM, which agrees well with the theoretical prediction in Section 2.4.

2.5.2   Array-based Photoacoustic Computed Tomography

Next, we demonstrate fast three-dimensional imaging of deeply seated 9L/*lacZ* tumor using an array-based photoacoustic computed tomography. The circular-scanning photoacoustic computed tomography is slow in imaging speed. It takes a single photoacoustic measurement at a time, and requires firing hundreds of laser pulses to get an image. By contrast, an ultrasonic array can acquire photoacoustic data simultaneously through a large number of parallel detection channels. As a result, an array-based photoacoustic tomography could obtain one image with a single laser shot, and improves the imaging speed by more than 2 orders of magnitude.

Figure 2.4(a) is the photograph of the imaged nude mouse taken before imaging. 9L tumors with and without *lacZ* transgene were grown in its right and left flanks, respectively. Both tumors were injected with the same amount of X-gal before imaging. After the mouse was sacrificed after experiment, we removed the skin on top of the tumors, and found only the *lacZ*+ tumor was stained blue, which further confirms the specificity of the detection of the *lacZ* expression by the chromogenic X-gal probe [Figure 2.4(b)]. The tumor-bearing region of the mouse was imaged *in vivo* with both photoacoustic and ultrasonic imaging. Figure 2.4(c~e) show the composite dual-modality

32

images in volumetric visualization, a cross-sectional view, and the projection view, respectively. Therein, photoacoustic images are colored green, while ultrasonic images are colored in gray scale. Figure 2.4(c) shows we could localize the *lacZ*+ tumor in three dimensions. Also, we observed that although tumor showed as a hypoechoic area in ultrasonic images, the lack of ultrasonic scattering is not a specific indicator for tumor [Figure 2.4(d)]. By contrast, using the *lacZ*/X-gal reporter strategy, PAI could detect the *lacZ*-marked tumor with a high specificity [Figure 2.4(e)]. In addition, by overlaying chicken breast tissue on top of the tumor, we found the expression of *lacZ* remains visible at a depth of 5.0 cm in biological tissue with a contrast-to-background ratio of 2.5. This proved the advantage of PAI over other optical molecular imaging techniques, such as BLI and FLI, in penetration depth. In addition, all images were obtained by averaging over 100 measurements, but using a low optical energy at 1/10 of the ANSI exposure limit. Assuming noise was uncorrelated between measurements, we could potentially obtain images with the same quality at a speed of 10 frames/second using the maximal laser energy allowed by the ANSI standard. The imaging speed can be further improved by adopting a high-repetition laser.
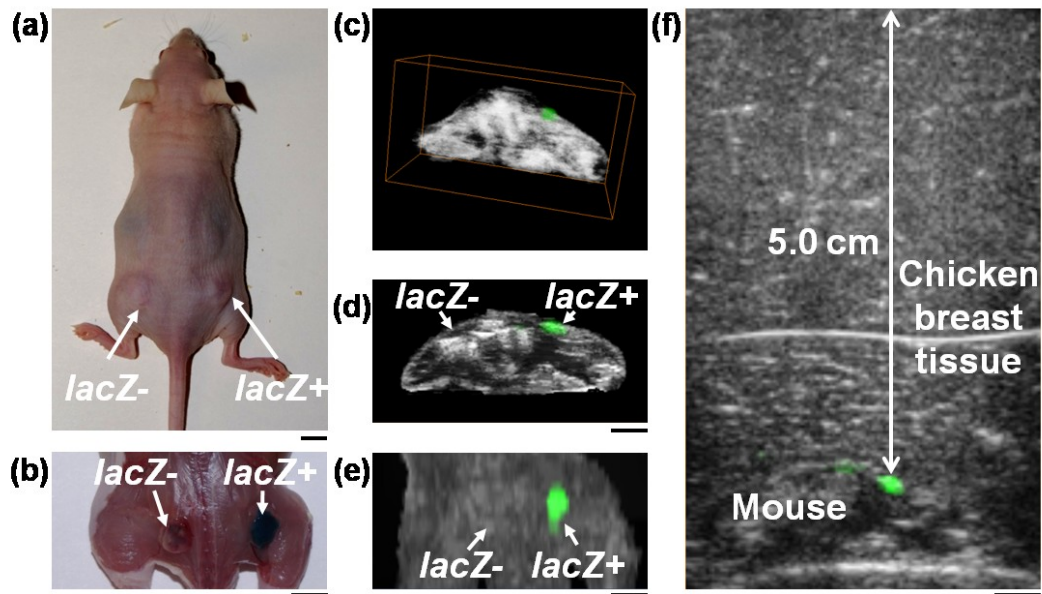
Figure 2.4 Imaging 9L tumors with and without the *lacZ* reporter gene by an array-based photoacoustic computed tomography and ultrasonic imaging system. (a) Photograph of a tumor-bearing mouse before imaging. (b) Photograph of the *lacZ-* and *lacZ+* tumors by removing the above skin after euthanasia. Composite photoacoustic and ultrasonic images shown in (c) three-dimensional visualization, (d) a typical B-scan, and (e) the maximum amplitude projection view. (f) B-scan image showing the *lacZ-*marked tumor can be imaged at 5-cm depth in biological tissue by overlaying chicken breast tissue on top of a mouse. Photoacoustic images are colored green, while ultrasonic images are colored in gray scale. The scale bars represent 5 mm.

2.5.3 Acoustic-resolution Photoacoustic Microscopy

We further demonstrated simultaneous imaging of *lacZ*-marked tumor and its surrounding microvasculature by dual-wavelength acoustic-resolution photoacoustic microscopy. Remodeling of microcirculation plays an important role in oncology. Although photoacoustic computed tomography is able to detect the *lacZ*-marked tumor at great depth, it lacks the resolving power to visualize the microcirculation system associated with the tumor. Acoustic-resolution photoacoustic microscopy uses high-

34

frequency focused transducer, and could achieve sufficient resolving power to visualize microvasculature at the cost of imaging depth. When operating at 50 MHz ultrasonic frequency, it penetrates ~3 mm into biological tissue with a lateral resolution of 45 µm and an axial resolution of 15 µm.

Blood vessels and the blue product have well-separated absorption peaks, and can be separately visualized by PAI at different optical wavelengths (Figure 2.2). Two wavelengths (584 nm and 635 nm) were selected to maximize the difference between the optical absorption of hemoglobin and the blue product within the efficient emission band of the DCM laser dye. The 584-nm wavelength was used to visualize the microvasculature. It is an isosbestic spectral point of hemoglobin, where HbO_2 and Hb have identical molar extinction coefficients, which dominate that of the blue product by a 5.4:1 ratio. The photoacoustic amplitude in the image acquired at 584 nm directly correlate with the local total hemoglobin concentration. The 635-nm wavelength was selected to map the *lacZ*-marked tumor, where the molar extinction coefficient of the blue product was 20.4 times greater than HbO_2's and 2.2 times greater than Hb's. Although this difference becomes bigger at longer wavelengths, the laser output was strongest at 635 nm.

The *lacZ*-marked 9L gliosarcoma was clearly visualized in the photoacoustic image acquired at 635 nm [Figure 2.5(a)]. By contrast, the morphology of the surrounding microvasculature was mapped in great details in the MAP image taken at 584 nm [Figure 2.5(b)]. The photoacoustic signal in Figure 2.5(b) represents the relative value of total hemoglobin concentration, a key parameter of the local metabolism. A combined pseudo-

colored image [Figure 2.5(c)] shows the spatial relation between the tumor and the surrounding microvasculature. From it, we were able to identify several tumor feeding vessels, which are indicated by arrows in Figure 2.5.

Furthermore, we were able to assess the expressional level of *lacZ* in the tumor. Under the assumption of uniform local optical fluence, the amplitude of the photoacoustic image is linearly proportional to the local absorption coefficient, which is the product of molecule's concentration and its molar extinction coefficient. In Figure 2.5(a), the photoacoustic amplitudes from the *lacZ*-marked tumor and the residual blood vessels were estimated to have a 4.0:1 ratio. The concentration of hemoglobin in normal blood is ~2.3 mM. Assuming blood has an oxygen saturation level of 90% and taking into account the aforementioned relations among molar extinction coefficients, we estimated the concentration of the blue product to be ~ 840 μM in the tumor. Given efficient delivery of X-gal, this estimated concentration of blue product will positively correlate with the concentration of β-galactosidase, i.e., the expression level of *lacZ* gene. Also, the tumor image in Figure 2.5(a) had low background, excluding the residual blood vessels. We estimated that the stained tumor was imaged with a contrast-to-background ratio (CBR) of ~36.6 dB. Hence, the minimum detectable concentration of blue product (with CBR = 1) was less than 12.3 μM. The detection threshold of the real expression product, β-galactosidase, was expected to be several orders of magnitude lower than this value.
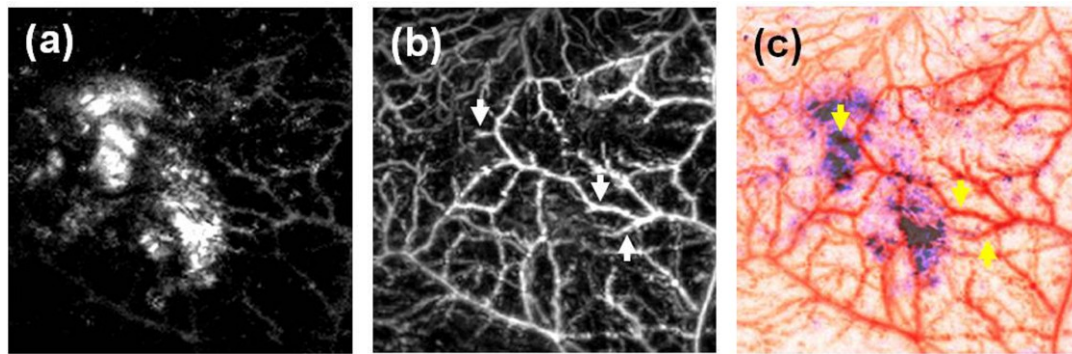
Figure 2.5   Simultaneously imaging a *lacZ*-marked tumor and its associated microvasculature by dual-wavelength acoustic-resolution photoacoustic microscopy. (a) MAP mage acquired at 635 nm showing tumor morphology. (b) MAP image acquired at 584 nm showing microvasculature. (c) Composite pseudo-colored image showing the spatial relations between tumor and blood vessels. Red: Blood vessels. Blue: tumor. Arrows indicate feeding vessels of tumor. Images are 10 mm × 10 mm.

2.5.4   Optical-resolution Photoacoustic Microscopy

Finally, we briefly show the sub-cellular localization of the *lacZ* expression using optical-resolution photoacoustic microscopy. By confining photoacoustic excitation by tight optical focusing, optical-resolution photoacoustic microscopy has been proven to obtain a lateral resolution at a fraction of a micron [28], and could potentially play an important role to study molecular biology in cultured cells.

Figure 2.6 shows photoacoustic images of a layer of fixed 9L/*lacZ* cells after staining in 1 mg/ml X-gal solution at 37˚C for 2 hours. We observed that, 9L/*lacZ* cells were between 20 ~ 40 µm in diameter. Inside cells, strong absorbers were scattered surrounding low-scattering absorbing centers that probably are cell nuclei. This implies that, β-galactosidase, the final product of *lacZ* expression, exists mostly in cytoplasm.

37
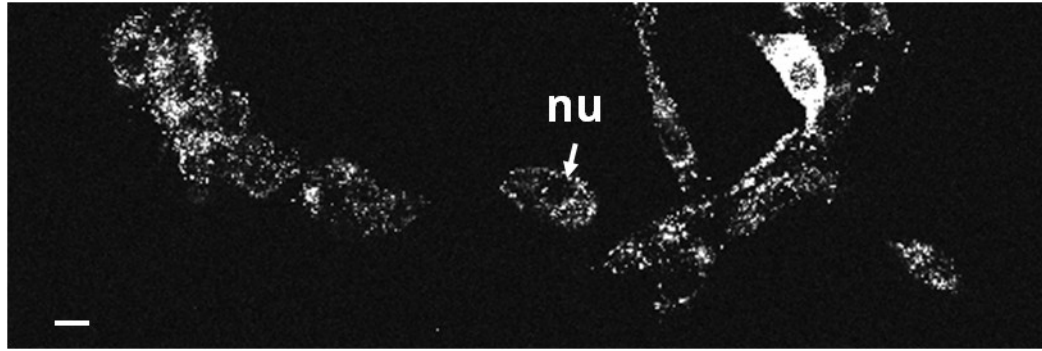
Figure 2.6 Imaging 9L/*lacZ* cells stained with X-gal by optical-resolution photoacoustic microscopy. nu: cell nucleus. The scale bar represents 10 µm.

2.6 Conclusion

In summary, we presented a new paradigm of molecular imaging to visualize the expression of a gene *in vivo* based on optical absorption by photoacoustic imaging. As the first demonstration, we successfully imaged the expression of the widely used *lacZ* reporter gene using multi-scale PAI systems in cells and living mice and rats, using a sensitive colorimetric probe, X-gal. We further demonstrated several merits of photoacoustic molecular imaging. We proved the expression of *lacZ* can be detected by PAI as deep as 5.0 cm in biological tissue. In addition, we showcased that PAI could follow the gene expression at multiple length-scales. We expect PAI could potentially become the important link between biological studies in the microscopic and macroscopic levels, which is currently absent in biomedical research. This work represents one of the pioneering efforts to extend photoacoustic methods for molecular imaging. With the future development of new chromogenic reporter gene systems,

photoacoustic reporter gene imaging will impact on both laboratorial research and clinical practice.

Methods:

Cell culture   The wild-type 9L rat gliosarcoma cell line was a generous gift from Dr. Michael Welch's laboratory in the School of Medicine of Washington University in St. Louis. The 9L/*lacZ* cell line was created by transfecting the 9L cell with BAG replication deficient retroviral vector carrying the *E. Coli lacZ* gene. The 9L/*lacZ* cells were purchased from American Type Culture Center (Manassas, VA). Cells were cultured in a growth medium of 90% of DMEM with 4.5 g/L glucose, and 1 mM sodium pyruvate and 10% of fetal bovine serum.

Preparation of the native cell lysate After removing the growth medium, the cultured 9L/*lacZ* cells were rinsed by 1× PBS and then collected into a 15 ml centrifuge tube. The cells were harvested after centrifuging at 3,200 rpm at 4°C for 5 minutes and discarding the supernatant. Then, we mixed ice-cold RIPA lysis buffer (Sigma-Aldrich, St. Louis, MO) with the cells, and incubated them in ice for 40 minutes. During the incubation, the solution was re-suspended every 10 minutes. Finally, the solution was centrifuged at 27,000 g for 20 minutes at 4°C. The supernatant was collected as the lysate of 9L/*lacZ* cells, which contains the active natively expressed β-galactosidase.

Animal preparation for imaging   For tumor inoculation, 5 µl suspension containing 5 million wild-type 9L or 9L/*lacZ* cells was injected under the skin of anaesthetized

39

animals using 0.3-ml syringe with a 29-gauge needle. Tumors were left to grow and monitored on a daily basis. Imaging was performed after the progression of the tumor became obvious. Hair was removed before experiments. For detecting the expression of *lacZ*, ~0.4 mg of X-gal in 20 µl PBS and DMSO (1:1) was injected close to the tumor 1 day ahead of imaging. During imaging, animals were kept asleep by a gas mixture of oxygen and 1% isoflurane at a flow rate of 1 L/min, and their blood oxygenation and heart rates were closely monitored. All animals recovered naturally after experiments without noticeable photodamage.

Circular-scanning photoacoustic computed tomography [17, 23]   A dye laser (ND6000, Continuum) with DCM laser dye, pumped by a Q-switched Nd:YAG laser, emitted light at 650 nm. Before reaching the animal, the light was broadened by a concave lens and a ground glass. The illumination was measured to be ~5 mJ/cm^2 on the skin surface. A single-element ultrasonic transducer (V323-SU, Panametrics-NDT. Central frequency: 2.25 MHz) was mechanically scanned around a circle surrounding the animal with 240 steps. Signals were amplified, digitized and averaged for 50 times at each scan position. A photodiode (DET110, Thorlabs) was used to compensate for fluctuations in the illuminating energy. Images were reconstructed using a modified back-projection algorithm [97]. By imaging a crossed-hair phantom, the in-plane spatial resolution was estimated to be ~400 µm [23]. It took ~25 minutes to acquire one image.

Array-based photoacoustic computed tomography [98]   This system is capable of performing both photoacoustic and ultrasonic imaging of the same sample. Photoacoustic signal was excited by 6.5-ns laser pulses at 10-Hz repetition rate generated by a tunable

dye laser (NS, Sirah) pumped by a Q-switched Nd:YAG laser (PRO-350-10, Newport). The light was delivered to the sample by a bifurcated optical fiber bundle (CB18043, Fiberguide). The acoustic signal was detected by a 128-element ultrasonic linear array with a nominal bandwidth of 4~8 MHz (L8-4, Philips Healthcare). The ultrasonic array and optical fiber bundle were assembled in a hand-held probe. The probe was scanned by a manual translation stage along the elevational direction to obtain a volumetric dataset. For each frame of photoacoustic image, measurements were averaged for 100 times, and took us 10 s to acquire. Photoacoustic and ultrasonic data were acquired sequentially with a modified clinical ultrasound imaging system (iU22, Philips Healthcare). Both photoacoustic and ultrasonic images were reconstructed using a Fourier-domain beam-forming algorithm [99]. For imaging the expression of *lacZ*, the dye laser was loaded with DCM dye, and emitted at 650 nm. Light fluence on the surface was measured to be ~2 mJ/cm^2, 10 times lower than the ANSI safety limit (20 mJ/cm^2).

Acoustic resolution photoacoustic microscopy [18, 24]   A tunable dye laser (ND6000, Continuum), pumped by a Q-switched Nd:YAG laser (Brilliant, Bigsky), provided laser pulses at two different wavelengths, 584 nm and 635 nm. Each laser pulse had a duration of 6.5 ns, and a pulse repetition rate of 10 Hz. The laser output was delivered to the imaging system through a multimode optical fiber with a 600-μm core diameter. The light coming out of the fiber was first expanded by a conical lens to form an annular beam and then weakly focused into the tissue, with its focal region coaxially overlapping the focus of a high-frequency ultrasonic transducer (V214-BCRM, Panametrics. Central frequency: 50MHz). The incident energy density at the tissue surface was controlled to be under 6 mJ/cm^2, which was well within the ANSI safety

41

standard. By using dark-field illumination with an incident angle of 45°, the strong acoustic waves otherwise emitted from structures close to the skin were reduced, which allowed us to image deeper structures better. The transducer had a central frequency of 50 MHz, a nominal bandwidth of 70%, and an NA of 0.44. It was immersed in water inside a tank with an opening at the bottom that was sealed with a thin transparent plastic membrane. The photoacoustic signal received by the transducer was amplified and then recorded by a digital oscilloscope (sampling rate: 250 MHz). At each lateral position, the data acquisition lasted for 2 μs, without averaging. A mechanical stage drove the raster scanning of the imaging probe to obtain a volumetric dataset. The acquired data was first processed by a synthetic-aperture focusing technique [100] to correct for the blurring outside the ultrasonic focus. The maximum photoacoustic amplitudes along each axial line were then projected on the skin surface, to form a maximum-amplitude projection (MAP) image. In previous experiments, the current system was quantified to have a lateral resolution of 45 μm and an axial resolution of 15 μm, and was capable of imaging ~3 mm deep into the skin [18].

Optical-resolution photoacoustic microscopy [101]   For photoacoustic excitation, a compact diode-pumped Nd:YVO4 laser (SPOT 100-532, Elforlight, UK. Maximal pulse repetition rate: 50 kHz) generates 1.2-ns pulses at the wavelength of 532 nm. The light was delivered to the imaging probe by a single-mode optical fiber. The light coming out of the fiber was first collimated, then focused into a diffraction-limited spot inside the tissue by the optical objective with a NA of 0.6. The generated photoacoustic signal was detected by the ultrasonic transducer (with a central frequency of 40 MHz and a numerical aperture of 0.5) in transmission mode. The signals were then amplified and

42

digitized at a sampling rate of 1 GHz. The objective and the transducer were mechanically scanned in raster mode in the x-y plane by two-axis step-motor driven linear stages. After scanning, a maximum-amplitude projection (MAP) image was obtained by projecting the maximum amplitude of each time-resolved signal onto the x-y scanning plane. The lateral resolution of this set-up was previously quantified to be 0.40 μm [28].

Chapter 3   Integrated Photoacoustic and Optical Coherence Microscopy (iPOM)†

3.1   Motivation

Microcirculation is vital to sustain human health, and disturbed microcirculation is involved in most pathological processes [102]. Existing microscopic imaging techniques, although they have greatly facilitated our understanding of morphology, function and regulation of normal and pathological microcirculation, suffer from several limitations. Intravital microscopy [103] and orthogonal polarization spectral imaging [104] lack depth resolution, and thus are unable to visualize three-dimensional morphology of microvasculature. Confocal and multiphoton microscopy [105, 106], although they can image tissue in three dimensions, generally require invasive introduction of exogenous fluorescence contrast agents.

In this chapter, I summarized our development of a novel multi-modality optical microscopy, the integrated photoacoustic and optical coherence microscopy (iPOM), which overcomes these problems and is capable of providing comprehensive information about microcirculation using endogenous contrasts.

---

† Reprinted with permission from L. Li, K. Maslov, G. Ku, and L. V. Wang, "Three-dimensional combined photoacoustic and optical coherence microscopy for in vivo microcirculation studies," Optics Express 17, 16450–16455 (2009).

iPOM combines photoacoustic microscopy (PAM) and optical coherence tomography (OCT) in a single system. When designed properly, OCT and PAM can have comparable imaging depths and spatial resolutions, which are suitable for microscopic imaging. More importantly, PAM and OCT has naturally complementary imaging contrasts. PAM is sensitive to optical absorption, and can provide detailed morphology of microvasculature. Based on multi-wavelength measurements, PAM can quantify the local total concentration of hemoglobin and blood oxygenation in each single vessel. OCT exploits the optical scattering contrast, and can provide real-time, *in vivo* biopsy of tissue with μm-order resolution. Based on the Doppler effect, depth-resolved profile of blood flow can be estimated. Combining the merits of the two, iPOM not only can reveal the morphological relation between the microvasculature and its surrounding tissue, but also can quantify important functional parameters of each single vessel, like the total concentration of hemoglobin, local blood oxygen saturation level and volumetric blood flow. What's more, with future development, iPOM could potentially quantify some novel important functional biomarkers of diseases, such as the local oxygen metabolic rate. We expect iPOM will have an impact not only on basic biomedical research, but also on clinical practice and pharmaceutical drug development.

3.2   System Design

Figure 3.1 illustrates our design of the current prototype of iPOM. It integrates optical-resolution PAM and spectral-domain OCT in a single imaging platform.

The source of OCT is a broadband superluminescent diode (D890, Superlum, Ireland. Central wavelength: 890 nm, FWHM bandwidth: 150 nm). For photoacoustic excitation, a compact diode-pumped Nd:YVO4 laser (SPOT 100-532, Elforlight, UK. Maximal pulse repetition rate: 50 kHz) generates 1.2-ns pulses at the wavelength of 532 nm. Light irradiating both OCT and PAM sub-systems is delivered to a shared imaging probe (dashed box in Figure 3.1) through single-mode optical fibers. After coming out of the fibers, light is collimated, combined by a cold mirror and focused into the tissue by an achromatic lens (AC-254-035B, Thorlabs, Newton, NJ). The OCT sub-system collects the backscattered photons from a sample back into the fiber coupler, mixes them with the light reflected by a reference mirror, and records their interference using a custom-made spectrometer. The profile of depth-resolved reflectivity of the sample is then obtained by Fourier transform of the recorded spectra after compensation for the dispersion difference between two arms, and re-sampling into the linear-k domain. The photoacoustic wave is reflected sideway by a glass slide and detected by a cylindrically focused ultrasonic transducer (Alpha series, GE Inspection Technology, Pomona, CA. Central frequency: 25 MHz. Focal length: 18 mm). A galvanometer (GVS001, Thorlabs, Newton, NJ) was applied to scan the optic focus along the ultrasonic focal line (x-axis). To acquire a volumetric imaging, the imaging probe is loaded on a precision linear stage (LS-65, Micos, Irvine, CA) and scanned along the y-axis.

We use an analog output card (NI 6713, National Instruments, Austin, TX) to generate timing signals (dashed lines in Figure 3.1) to synchronize firing of the pulsed laser, galvanometer and stage scanning, PAM and OCT image acquisition. Currently, at each lateral position, the OCT data is first integrated for 150 µs and downloaded by a frame

grabber (Horizon Link, i2S, Cos Cob, CT). Then the photoacoustic signal is sampled at 200 MHz for 1 μs by a high-speed digitizer (NI 5124, National Instruments, Austin, TX). As a result of the interleaved acquisition, PAM and OCT images are inherently registered. During image acquisition, the most recent PAM and OCT B-scan images (x-z slice) are displayed on the computer screen in real time, which intends to help guide physicians to quickly locate regions of interest in clinical applications. The system control, data acquisition and on-screen visualization were implemented on a single commercial workstation driven by a custom-written multi-threading VC++ code.

Compared with the optical-resolution PAM previously reported in Ref. [19], our iPOM system has advantages in imaging speed and flexibility In the previous system, the bottleneck of imaging speed is the slow mechanical scanning of probes across both lateral directions. iPOM overcomes this obstacle, and scans the optical focus by a galvanometer along the x-axis at a much faster speed. Now, the frame rate of iPOM is limited by the maximum pulse repetition rate where the pulsed laser can provide enough pulse energy out from the single-mode fiber for photoacoustic excitation. Using the current pulsed laser, we are able to obtain dual-modality images at a speed of 5,000 A-lines/second. A B-scan image comprising 800 A-lines can be repeated at ~6 frames/second. A typical volumetric dataset with 800 × 800 A-lines takes ~ 2 minutes to acquire, which is more than 5 times faster than previous system. Also, in iPOM, the light for imaging was delivered to the probe through flexible optical fibers, which allow us to adapt this system to a portable set-up in the future for intraoperative applications. In both PAM and OCT images, the lateral resolution is determined by the width of the optical focus, which was estimated by imaging a USAF-1951 resolution test chart to be better than 3.5 μm in the

47

focal zone. The axial resolutions of PAM and OCT are determined by the bandwidth of the ultrasonic detection and light source, respectively. We estimated them to be ~31 μm in PAM images, and ~3.5 μm in OCT images.
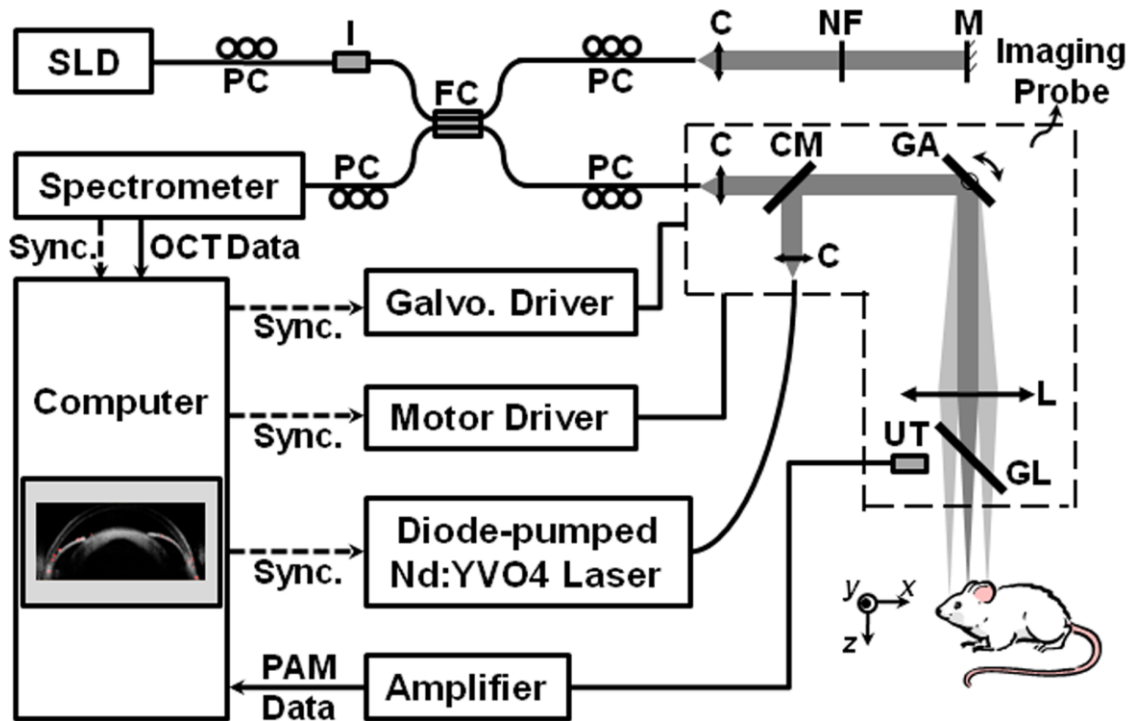
Figure 3.1 Schematic of the integrated photoacoustic and optical coherence microscope (iPOM). SLD: superluminescent diode; PC: polarization controller; I: isolator; FC: 80/20 2×2 fiber coupler; C: collimator; NF: neutral density filter; M: mirror; CM: cold mirror; GA: galvanometer; L: achromatic lens; UT: ultrasonic transducer; GL: glass plate.

3.3 Demonstration of Potential Biomedical Applications

3.3.1 Imaging a Mouse Ear

We first demonstrated the capability of iPOM by imaging mouse ears *in vivo* using a transmission-mode prototype [63]. Nude mice (Harlan, Indianapolis, IN. Weight: ~30 g) were used in our experiments.

Figure 3.2 shows that the *x-y* projection images of a nude mouse ear obtained *in vivo* by iPOM correlate well with the photograph taken through an optical transmission microscope with 4× magnification. OCT and PAM visualized different aspects of the tissue better than the traditional optical microscope. In the OCT image [Figure 3.2(a)], the sebaceous glands are resolved with higher resolution, due to the better rejection of background scattered light. The PAM image [Figure 3.2(b)] clearly maps the microvasculature at higher contrast in greater details than the photograph. The average contrast-to-background ratio between blood micro-vessels and surrounding tissue was estimated to be ~25:1, which manifests the advantage of the absorption-based photoacoustic method in imaging microvascular morphology. In Figure 3.2(c), we co-registered the two images, with the blood vessels in red and avascular structures in gray scale.
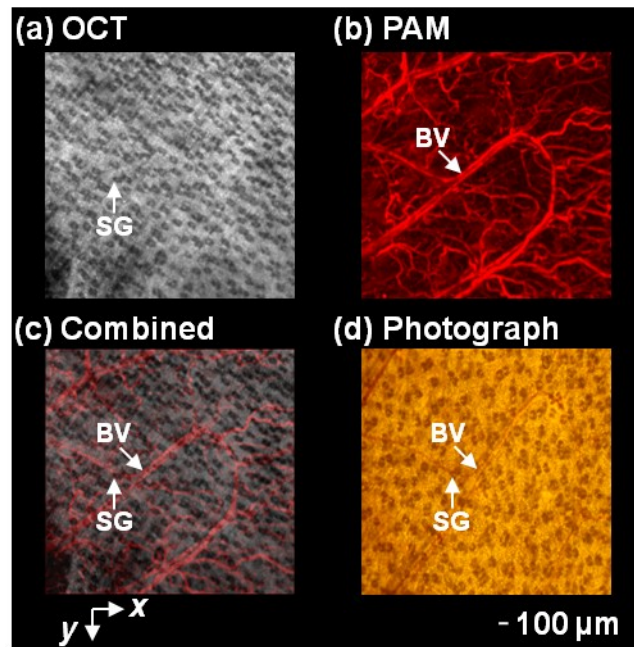
Figure 3.2 iPOM images of a nude mouse ear (x-y projection) (a) OCT. (b) PAM. (c) Overlay dual-modality images. (d) Photograph taken through an optical microscope. SG: sebaceous gland; BV: blood vessel.

The benefits of combining the complementary contrasts of OCT and PAM can be better appreciated by looking at a cross-section of tissue. To achieve axial resolution, PAM records the time-of-flight of sound, whereas OCT uses coherence gating. Figure 3.3 shows typical cross-sectional images of a nude mouse ear acquired by iPOM at a fixed y position, where the ventral side of the ear appears on the top. OCT provided us a microanatomy of the avascular structures in the ear [Figure 3.3(a)]. From the OCT cross-sectional images, we were able to estimate that the imaged regions had a thickness varying from 200 to 300 μm. Both OCT and PAM could see through the entire thickness of the mouse ear. By comparison with typical histology, we were able to identify various structures in the ear. The ear consisted of two skin layers separated by a layer of non-scattering cartilage. The epidermis, the outmost layer of the skin, tended to be more

scattering. The weak-scattering regions embedded in the skin layers were most likely sebaceous glands. We found more sebaceous glands in the dorsal skin layer than in the ventral layer, which agreed well with previous reports [107]. However, blood vessels were not evident on the OCT image. By contrast, PAM [Figure 3.3(b)] is good at locating micro-vessels in the ear, with little information about the surrounding tissue forming the local environment of vessels. Some vessels, such as the one labeled as CP, had a diameter of ~ 7 µm, and were believed to be capillaries. From the co-registered cross-sectional image [Figure 3.3(c)], we could identify the anatomical location of each imaged vessel. It was observed that the smallest vessels were located close to the skin surface. Other layers of vasculature were found near the cartilage layer. More interestingly, a large number of vessels were found to surround sebaceous glands, as reported earlier [107].
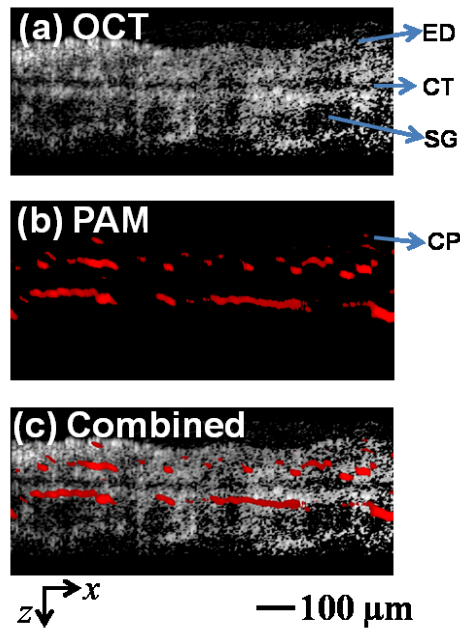
Figure 3.3 iPOM images of a nude mouse ear (x-z cross-section). (a) OCT. (b) PAM. (c) Overlay the dual-modality images. ED, epidermis; CT, cartilage; SG, sebaceous gland; CP, capillary.

Both PAM and OCT are intrinsically three-dimensional imaging modalities. In order to obtain a volumetric dataset, iPOM only needs two-dimensional raster scanning, unlike confocal and multi-photon microscopes, which depend on three-dimensional scanning. The three-dimensional PAM image [Figure 3.4(a)] reveals details of the shape, direction, branching and connectivity of blood micro-vessels. Figure 3.4(b) shows a top view of the volumetric rendering of the dual-modality dataset, where the microscopic epidermal ridges are evident from the OCT contrast. The distinguishable vascular morphologies in the ventral and dorsal layers of the skin are also compared in Figure 3.4(c) and (d).
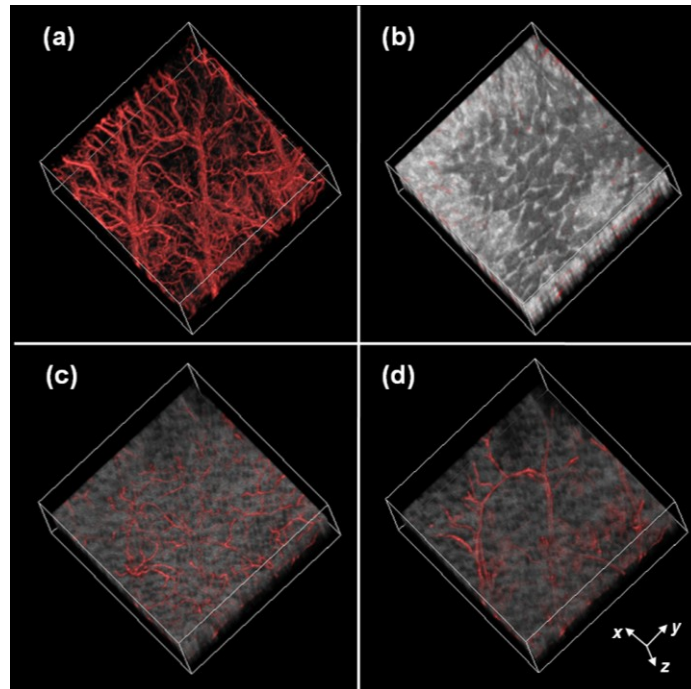
Figure 3.4 iPOM images of a nude mouse ear (3-D visualization). (a) PAM image of the microvasculature only; (b) Dual-modality image showing the skin surface, a top view; (c) Dual-modality image showing the microvasculature in the ventral skin layer, a top view from 88 μm below the skin surface; (d) Dual-modality image showing the microvasculature in the dorsal skin layer, a top view from 148 μm below the skin surface. The micro-vessels imaged by PAM are colored in red, while avascular tissues imaged by OCT are in gray. The bounding box has dimensions of 3.6 mm x 3.6 mm x 0.4 mm.

3.3.2   Imaging Mouse Skin

Cutaneous microcirculation was suggested to be a representative model for studying generalized mechanisms underlying microvascular functions and dysfunctions. Structural remodeling and functional disturbance of cutaneous microvasculature are involved in various cardiovascular diseases, and can be assessed to aid accurate diagnosis and optimized treatment [108]. We further explored the potential application of iPOM in studying cutaneous microcirculation, which may lead to its clinical translation.

We imaged the scalp of a Swiss Webster mouse (Harlan, Indianapolis, IN. Weight: ~20 g) *in vivo*. The PAM images are colored red, while the OCT images are rendered in gray scale. Figure 3.5(a) and (b) show the composite dual-modality images in the x-y projection view and the x-z cross-sectional view, respectively. iPOM not only sees details of the microvascular morphology down to single capillaries using photoacoustic detection, but also depicts the microanatomy of the surrounding tissue by OCT. By comparing OCT images against a photograph of a typical histological slice of a mouse scalp taken by a commercial optical microscope [Figure 3.5(c)], we found OCT clearly distinguished the striated structure of the skin, including the epidermis, the papillary and reticular dermis, as well as the subcutaneous tissue. The hair follicles and the attached sebaceous glands manifested themselves as weak-scattering dark areas inside the skin. More importantly, from the three-dimensional visualization of photoacoustic data, we observed that the cutaneous microvasculature was organized as two distinct horizontal plexuses. The first plexus mostly made of microvessels was located in the epidermal-
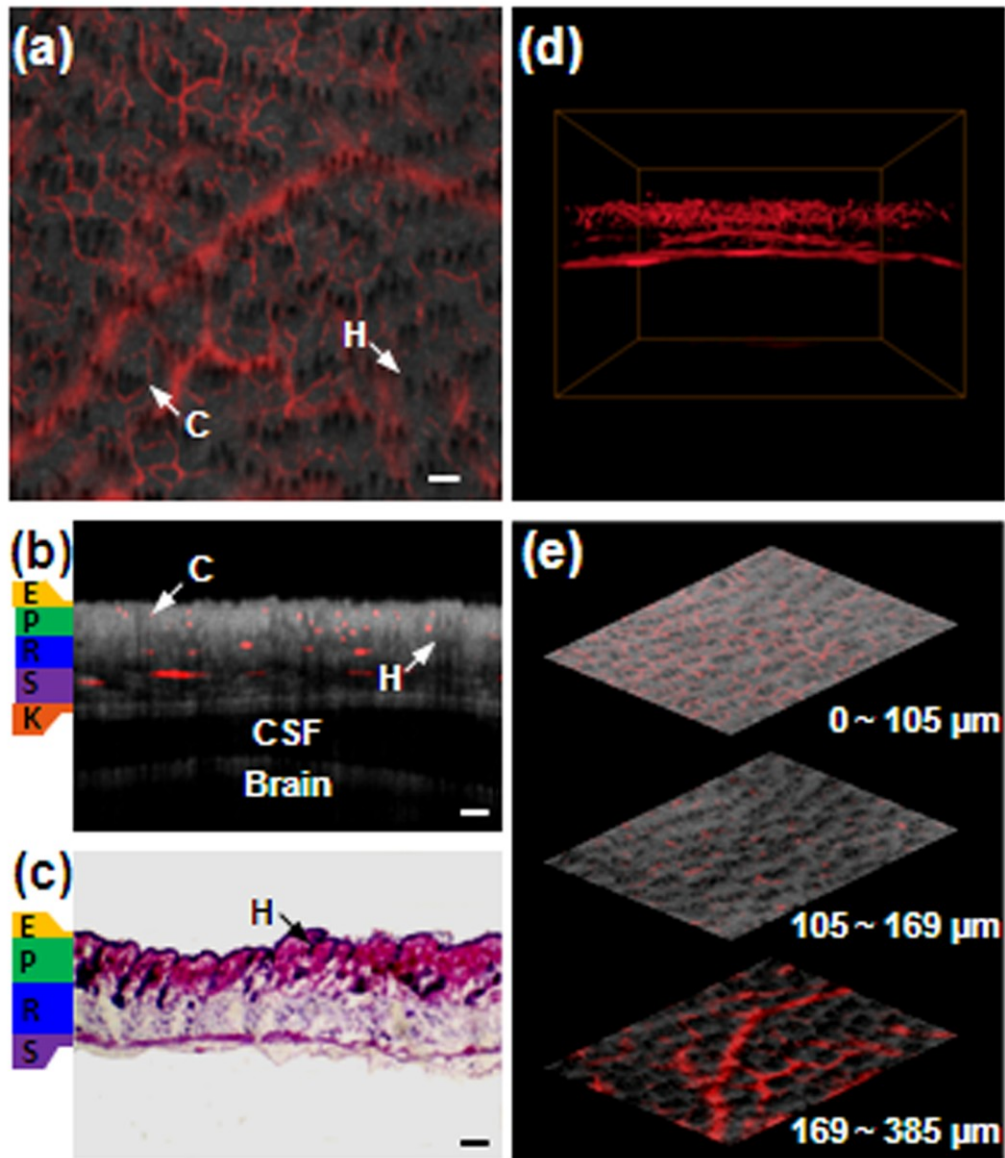
Figure 3.5 iPOM images of skin obtained *in vivo*. PAM images are colored red, while OCT images are colored in gray scale. (a) *x-y* projection view. (b) A typical B-scan image (*x-z* slice). (c) An H&E stained histological *x-z* slice for comparison. (d) 3D visualization of the cutaneous microvasculature. (e) *En face* images (*x-z* projection) of three sub-layers of the skin. The scale bars in (a), (b) and (c) represent 100 μm. The bounding box in (d) has a dimension of $2 \times 2 \times 1.5$ mm^3. Each image in (e) has a dimension of 2×2 mm^2. C: blood capillary; H: hair follicle; E: epidermis; P: papillary dermis; R: reticular dermis; S: subcutaneous tissue; K: skull.

dermal junction (within 105 µm under the skin surface), while the second layer comprising bigger vessels was at the dermal-subcutaneous junction (169 ~ 385 µm). The two were connected with blood vessels running mostly in the vertical directions. [See Figure 3.5(e)] This characteristic organization of cutaneous microcirculation was documented previously only through histology [109]. To the best of our knowledge, using iPOM, we are the first to be able to visualize these features *in vivo*.

3.3.3   Imaging the Anterior Segment of a Mouse Eye

OCT could detect ocular lesions based on morphological changes in both the retina and the anterior segment of the eye, and has become a major imaging tool in routine ophthalmological diagnosis. However, it is limited in term of evaluating physiological functions. Hence, invasive fluorescent angiography, which requires the introduction of exogenous fluorescence dyes, is still an essential tool for visualizing the morphology and functions of ocular microcirculation [110]. We expect iPOM could enable simultaneous structural and functional imaging of the eye using only endogenous contrasts, and could be a useful tool in ophthalmology.

Here, we demonstrated label-free imaging of the anterior segment of an eye of a Swiss-Webster mouse *in vivo* by iPOM. The PAM images are colored red, while the OCT images are rendered in gray scale. Figure 3.6(a), (b) and (c) show the composite dual-modality images of the eye in the x-y projection view, the x-z cross-sectional view and in 3-D, respectively. We see iPOM can only reveal the morphology of the cornea, iris, the front part of the lens and the ciliary body, but also map the ocular microcirculation

55

system mostly in the iris in great details. To obtain these images, we used a pulse energy of 60 nJ, which is well within the ANSI laser safety limit. We predict that, with further development of functional imaging capabilities, iPOM will impact our understanding and diagnosis of a wide range of eye diseases, such as glaucoma, diabetic microangiopathy, and ocular tumor.

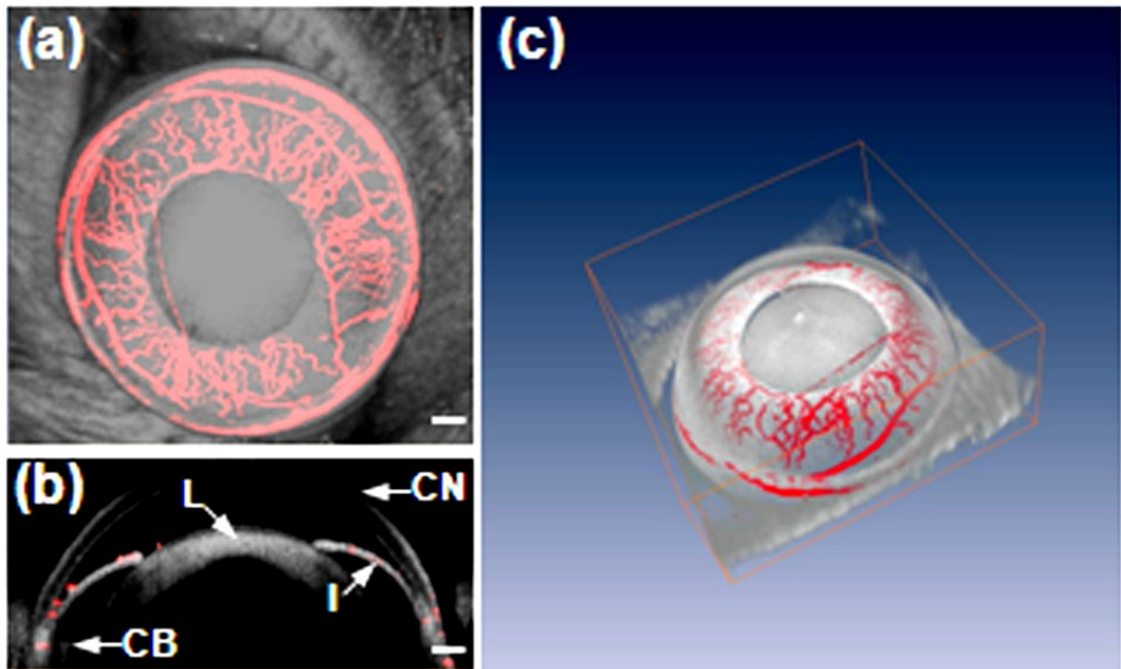Figure 3.6 iPOM images of the anterior segment of a mouse eye obtained *in vivo*. PAM images are colored red, while OCT images are colored in gray scale. (a) *x-y* projection view. (b) A typical B-scan image(*x-z* slice). (d) 3D visualization. The scale bars in (a) and (b) represent 200 μm. The bounding box in (c) has a dimension of $3.4 \times 3.4 \times 1.5$ mm^3. CN: cornea; L: lens; I: iris; CB: ciliary body.

3.3.4 Imaging Cell Infiltration in Scaffold

Tissue engineering is an emerging field to use engineered biological substitutes to restore, maintain, or enhance functions of tissues and organs [111, 112]. The replacement tissue is generally constructed by rationally growing cells on a three-dimensional porous scaffold, which provides mechanical support and biochemical microenvironment for tissue growth. To help optimizing the design of scaffolds, imaging tools that reveal the interactions between cells and scaffolds are highly desirable. We expect iPOM will be able to take this role and become a useful tool for facilitating tissue engineering.

As a preliminary demonstration, we demonstrated label-free chronic imaging of the infiltration of B-16 melanoma cells in Poly($_{D,L}$-lactide-*co*-glycolide) (PLGA) inverse opal scaffolds [113]. At day 0, B-16 cells were seeded on the upper surface of the scaffolds. Figure 3.7 shows iPOM images taken at days 1 and 7. B-16 cells contains strongly absorbing melanin, thus can be imaged by PAM. OCT can see the morphology of both the scaffold and cells. When making composite dual-modality images, we overlay PAM images (red) on top of OCT images (green). As a result, the area where cell grows will be red, while the skeleton of the scaffold remains green. Figure 3.7(a) shows that 1 day after seeding, most cells were attached to the wall of the pores in a relatively uniform manner. In day 7, cells proliferated towards the center of the pores in a non-uniform fashion [Figure 3.7(e)]. Compared with the photographs taken by commercial optical microscope [Figure 3.7(d) and (h)], we can better appreciate the advantage of PAM to see cells not only on the top of the scaffold but also inside the scaffold. Thanks to the depth sectioning capability of iPOM, we further observed that most cells were restricted to the upper

57

surface of the scaffold at day 1 [Figure 3.7(b) and (c)], while a large portion of cells

infiltrated to a depth of 200 µm into the scaffold at day 7 [Figure 3.7(f) and (g)].
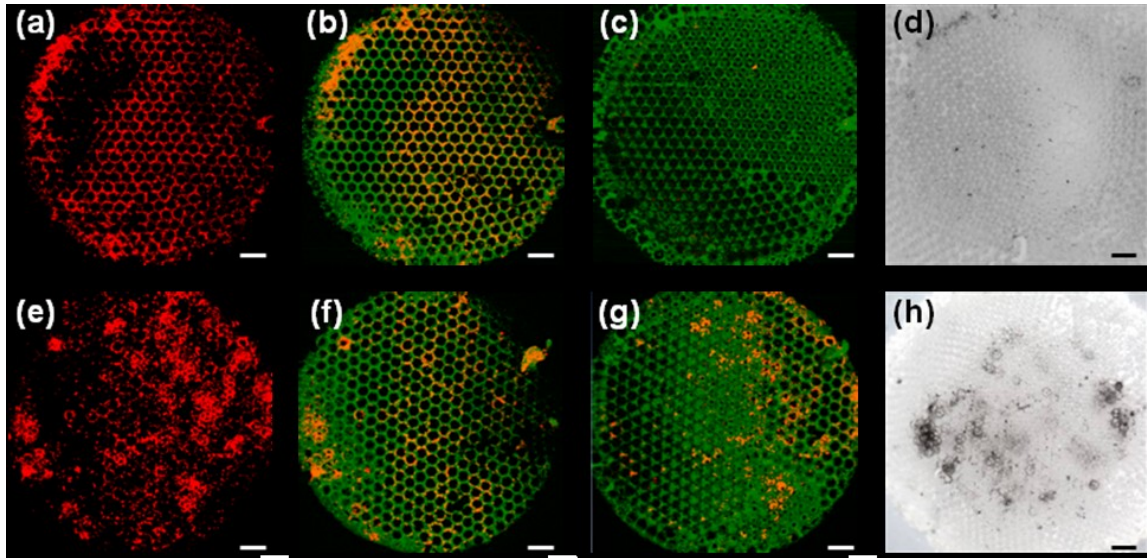
Figure 3.7 iPOM images of infiltration of B-16 melanoma cells in a PLGA inverse opal scaffold. PAM images are colored red, while OCT images are colored green. a,e: x-y projection PAM image. b,f: x-y cross-sectional dual-modality images at the upper surface of the scaffold. c,g: x-y cross-sectional dual-modality images at 200 µm deep. d,h: photographs taken with optical microscope. a~d taken at day 1. e~h taken at day 7. The scale bars represent 200 µm.

iPOM has an advantage to be able to image tissue and scaffold with different imaging

contrasts, thus is especially suited to study the interaction between the two. We predict

iPOM will find versatile applications in tissue engineering, such as investigating the role

of angiogenesis in engineered tissue, and monitoring the controlled degradation of

scaffold during tissue formation, etc.

3.4   Conclusion

In summary, we proposed a novel multi-modality microscopy, iPOM, which can provide comprehensive information about biological tissue using both optical absorption and scattering contrasts. We designed and built a high-speed reflection-mode prototype of iPOM, and further demonstrated its potential applications in studying cutaneous and ocular microcirculation, as well as tissue engineering.

Chapter 4 Optical Coherence Computed Tomography (Optical CCT)[‡]

4.1 Motivation

Optical coherence tomography (OCT) is an important biophotonic imaging technique, which can provide real-time high-definition *in vivo* biopsy of biological tissue (see Chapter 1). OCT assumes all detected photons are scattered only once at the depth that equals to one half of the measured pathlength. However, most biological tissues are strongly scattering to light. A photon will be scattered an average of 10 times during every 1-mm travel in normal soft tissue. Multiply scattered photons coming back from other part of tissue can also be collected by OCT with the same pathlength, thus are generally considered as noise that will blur OCT images. It was found that, with the increase in probe depth, the number of minimally scattered photons decreases exponentially, while the population of the multiply scattered photons increases. The latter group was estimated to become dominant somewhere beyond 500~700 μm deep in tissue [114]. As a result, the imaging depth of OCT is usually restricted to ~1 mm in highly scattering tissue like skin, and its image quality degrades quickly with the increase of probe depth. In addition, OCT is predominantly sensitive to optical scattering, which is

---

[‡] Reprinted with permission from L. Li, and L. V. Wang, "Optical coherence computed tomography," Applied Physics Letters 91, 141107 (2007).

60

associated with the microstructure of tissue instead of its molecular content. OCT is generally insensitive to other molecule-specific optical contrasts, such as absorption.

In this chapter, I summarized our invention of a novel optical tomography, named optical coherence computed tomography (optical CCT), in order to overcome the aforementioned restrictions in OCT. Similar to OCT, Optical CCT measures both singly and multiply scattered photons from tissue in a time-resolved manner using a low-coherence optical interferometer. Different from OCT, optical CCT produces an image of the optical properties of tissue using a reconstruction algorithm based on a photon migration model.

4.2   System Design

Figure 4.1 shows our design of the first prototype of optical CCT, which is configured as a fiber-optic Mach-Zehnder interferometer. The light emitted by a broadband superluminescent diode (IPSDD0803, InPhenix, Livermore, CA. Central wavelength λ_0=829 nm, bandwidth $\Delta\lambda$=36.4 nm) is split into two parts by a 90/10 fiber coupler. The first part is shaped by lenses L1 and L2 and focused onto one surface of the sample. Light, scattered once or multiple times in the sample, is collected from the opposing surface of the sample by lenses L3 and L4 into a second fiber coupler and interferes with the second part of source light that travels through the reference arm of the interferometer. Similar to spectral-domain OCT explained in Chapter 1, the interference signal is recorded as a spectrum by a home-made spectrometer, comprising a high-

resolution transmission gratings G, an imaging lens L8 and a high-speed line-scan camera (Aviiva M2, Atmel, San Jose, CA). The polarization and dispersion differences between the sample arm and reference are carefully compensated for. The time-resolved profile of the reemitted light is obtained from the recorded spectrum through Fourier transform as previously described in Chapter 1. The illumination and collection optics are pre-aligned coaxially. Both can be scanned laterally (in the x-y plane) by translation stages to take measurements through different illumination-detection pairs. This system can be easily parallelized, for example using a coherent optical fiber-bundle, in the future to increase the imaging speed. Using the current set-up, we can measure the reemitted light from the tissue with a temporal resolution equivalent to the coherence time of the source light, which is $0.88\lambda_0^2 / c\Delta\lambda = 56$ fs (c is the speed of light in vacuum). The temporal resolution can be further improved by increasing the bandwidth of the light source.
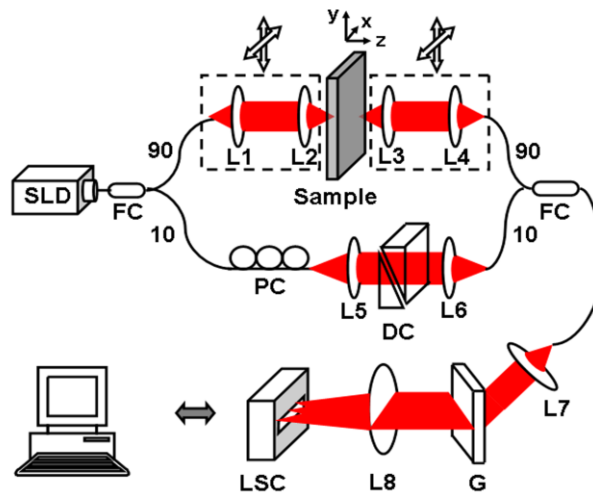
Figure 4.1 Schematic of optical coherence computed tomography (optical CCT) system. SLD: superluminescent diode; FC: fiber coupler; PC: polarization controller; DC: dispersion compensation; G: gratings; LSC: Line-scan camera; L1-8: lenses.

4.3   Reconstruction Algorithm

Photon migration in a biological tissue is believed to be governed by the radiative transfer equation (RTE), which can be written as

$$(\partial/c\partial t - \hat{s}\cdot\nabla - (\mu_a + \mu_s))L(\vec{r},\hat{s},t) - \mu_s\int_{4\pi}L(\vec{r},\hat{s}',t)P(\hat{s}'\cdot\hat{s})d\Omega' = S(\vec{r},\hat{s},t)_,\qquad(4.1)$$

where $L(\vec{r},\hat{s},t)$ is the radiance of the light at position $\vec{r}$ along the direction $\hat{s}$ with a total traveling time t. Ω' denotes the solid angle. S stands for the light-emitting source. μ_a and μ_s represent the absorption coefficient, the scattering coefficient of the tissue, while $P(\hat{s}'\cdot\hat{s})$ is the phase function of scattering that is related to the microstructure of tissue. [1]. As indicated in Equation (4.1), the light, reemitted after interaction with medium, carries information about important optical properties characterizing the medium, such as μ_a, μ_s and $P(\hat{s}'\cdot\hat{s})$.

As exemplified by DOT, a model-based reconstruction algorithm can be used to obtain a map of these optical properties in the medium from measurements of the reemitted light from tissue. The algorithm comprises two components: 1) a forward model, which solves the RTE (sometimes with proper simplifying assumptions) and computes the expected measurements from a spatial distribution of tissue's optical properties, and 2) an inverse procedure, which finds the distribution of these properties that matches the theoretical prediction of the forward model and the experimental measurement.

DOT works in the diffusive regime. The migration of diffusive photons can be forwardly modeled by simplifying RTE with the diffusion approximations. The resulted diffusion equation can be solved analytically [1]. In contrast to DOT, optical CCT will mostly work in the pre-diffusive regime, where the diffusion approximations no longer hold. Thus, we must resort to the full transient radiative transport equation (RTE) in Equation (4.1), which is much more challenging to solve.

As an initial demonstration of the concept of optical CCT, in this study we aim to image an absorbing object, which represents spatially distributed absorbing perturbation $\Delta\mu_a(\vec{r})$. Perturbations in scattering coefficient μ_s and the scattering phase function can be mapped by following similar procedures.

For imaging the small embedded absorber, we measure the temporal profile of the light coming out from the tissue through multiple illumination-detection pairs both with the absorbing object located therein, $T(\vec{r}_s,\vec{r}_d,t)$, and without the object located therein, $T_0(\vec{r}_s,\vec{r}_d,t)$. $\vec{r}_s$ and $\vec{r}_d$ are the illumination and detection locations on the surface of the medium, respectively. Given the lesion is small, the difference between the two measurements $\Delta T = T - T_0$ can be derived from Equation (4.1) under the first-Born approximation as

$$\Delta T(\vec{r}_s,\vec{r}_d,t)=-\iint_{\Omega_d V}\iint_{4\pi t'}\hat{n}(\vec{r}_d)\cdot\hat{s}_d S(\vec{r}_s,\hat{s}_s,t_s)G(\vec{r},\hat{s},t';\vec{r}_s,\hat{s}_s,t_s)\Delta\mu_a(\vec{r})G(\vec{r}_d,\hat{s}_d,t,\vec{r},\hat{s},t')dt\,d\Omega\,dV\,d\Omega_d$$

$$=\int_V\Delta\mu_a(\vec{r})\iint_{\Omega_d}\iint_{4\pi t'}-\hat{n}(\vec{r}_d)\cdot\hat{s}_d S(\vec{r}_s,\hat{s}_s,t_s)G(\vec{r},\hat{s},t';\vec{r}_s,\hat{s}_s,t_s)G(\vec{r}_d,\hat{s}_d,t,\vec{r},\hat{s},t')dt\,d\Omega\,d\Omega_d\,dV$$

$$=\int_V\Delta\mu_a(\vec{r})J(\vec{r};\vec{r}_s,\vec{r}_d,t)dV \qquad\qquad (4.2)$$

,

where $\Delta\mu_a$ represents the increase in absorption coefficient due to the existence of the absorbing object. $\hat{n}$ is the inward normal of the surface at $\vec{r}_d$, and G is the Green's function solution for Eq. 2. The integration involving S and G can be merged into a single function J, which links $\Delta\mu_a$ that we try to image, with measurements ΔT. $J(\vec{r};\vec{r}_s,\vec{r}_d,t)$ is often referred to as a sensitivity function, which physically means the rate of change in measurement ΔT as a result of an absorbing perturbation at $\vec{r}$. Thus, we simplified the forward problem for optical CCT into a linear equation given in Equation (4.2). Due to the discrete nature of measurements, the forward model can be further described in a matrix form as

$$\Delta\mathbf{T}=\mathbf{J}\Delta\mathbf{\mu_a}, \qquad\qquad (4.3)$$

where $\Delta\mathbf{T}$ is the vector representing the differential measurement from experiment, and has a total of N=(number of source-detection position pairs)×(number of pathlength segments) elements. $\Delta\mathbf{\mu_a}$ is the vector representing the increase of absorption coefficient in each voxel of the media, and has a total of M=(number of voxels) elements. $\mathbf{J}$ is the

discrete form of the sensitivity function times the volume of a voxel, and is an N×M matrix.

In practice, the sensitivity matrix $\mathbf{J}$ is obtained numerically by a time-resolved Monte Carlo simulator. We followed the general Monte Carlo method described in Ref. [115] with the following major modifications: 1) Tack the traveling time of every photon packet during propagation, and record the reemission at the detection surface into a matrix as a function both of position and time. 2) Use an auxiliary matrix to record voxels at r where scattering events occurs for each photon packet. When this photon packet emitted from the detection surface, the remaining weight divided by $(\mu_a+\mu_s)$ is added to the element of the sensitivity matrix $\mathbf{J}$ corresponding to the illumination-detection position pair, time and the voxel position r. The boundary conditions imposed in experiments were also taken into account in simulation.

To obtain an image of the object, we inverted measurements using a standard simultaneous iterative reconstruction technique (SIRT), which could be given in the matrix format as

$$\Delta\mathbf{\mu_a}^{k+1}=(\mathbf{I}-\mathbf{CJ^TRJ})\Delta\mathbf{\mu_a}^{k}+ \mathbf{CJ^TR\Delta T}, \qquad (4.4)$$

where k and k+1 are the indices of iteration. $\mathbf{R}=\text{diag}(r_i)$ and $\mathbf{C}=\text{diag}(c_i)$ are diagonal matrices of the inverse of the row and column sums of $\mathbf{J}=[a_{ij}]$, respectively, that is $r_i=1/\Sigma_j a_{ij}$ and $c_j=1/\Sigma_i a_{ij}$. The iterative inversion procedure begins with initial assumption that $\Delta\mathbf{\mu_a}^{0}=\mathbf{0,}$ and terminates until $\Sigma[(\Delta\mathbf{\mu_a}^{k+1}-\Delta\mathbf{\mu_a}^{k})^2]/\Sigma[(\Delta\mathbf{\mu_a}^{k})^2]$ falls below a certain preset threshold. The matrices $(\mathbf{I}-\mathbf{CJ^TRJ})$ and $\mathbf{CJ^TR\Delta T}$ do not depend on the position and optical properties of the hidden absorbing object, thus can be calculated before experiments and stored as a database to significantly reduce the computation time of the

66

reconstruction in real applications. In order to make the reconstruction less susceptible to the boundary condition of the object, $\mathbf{M_0}\Delta\mathbf{T}/\mathbf{T_0}$ instead of $\Delta\mathbf{T}$ is used for inversion, where $\mathbf{T_0}$ and $\mathbf{M_0}$ are the measurements obtained through experiment and simulation without absorbing inclusion, respectively. Also, an obvious priori that $\Delta\boldsymbol{\mu_a}$ is always positive was imposed during the iteration.

4.4   Experimental Results

4.4.1   Comparison Between Experimental Measurement and Theoretical Prediction

To validate the system, we first compared the optical CCT measurement of the reemitted light from a phantom with known optical properties against theoretical predictions by the time-resolved Monte Carlo simulator (Figure 4.2). We constructed a highly scattering tissue-mimicking phantom using aqueous suspension of 1-μm polystyrene microspheres. The optical properties calculated using the Mie theory were μ_s=113.6 cm^{-1} and scattering anisotropy g=0.90, whereas the absorption is negligible. The phantom used in our experiment was 2.6 mm thick, corresponding to ~30 scattering mean-free-paths. The integration time for recording a single spectrum was 1 ms. The temporal profile of light measured by a single source-detector pair was the average based on 500 recorded spectra to alleviate the speckle noise. Figure 4.2(a) shows the temporal profile of light detected at the source-detector pairs with lateral shift x ranging from -0.5 mm to 0.5 mm. The measurements at x=0 mm, 0.2mm, 0.4mm, after compensation for the depth-dependent decay due to the finite spectral resolution of the spectrometer, match the predictions from the Monte Carlo simulation well, shown in Figure 4.2(b), (c) and (d).

67
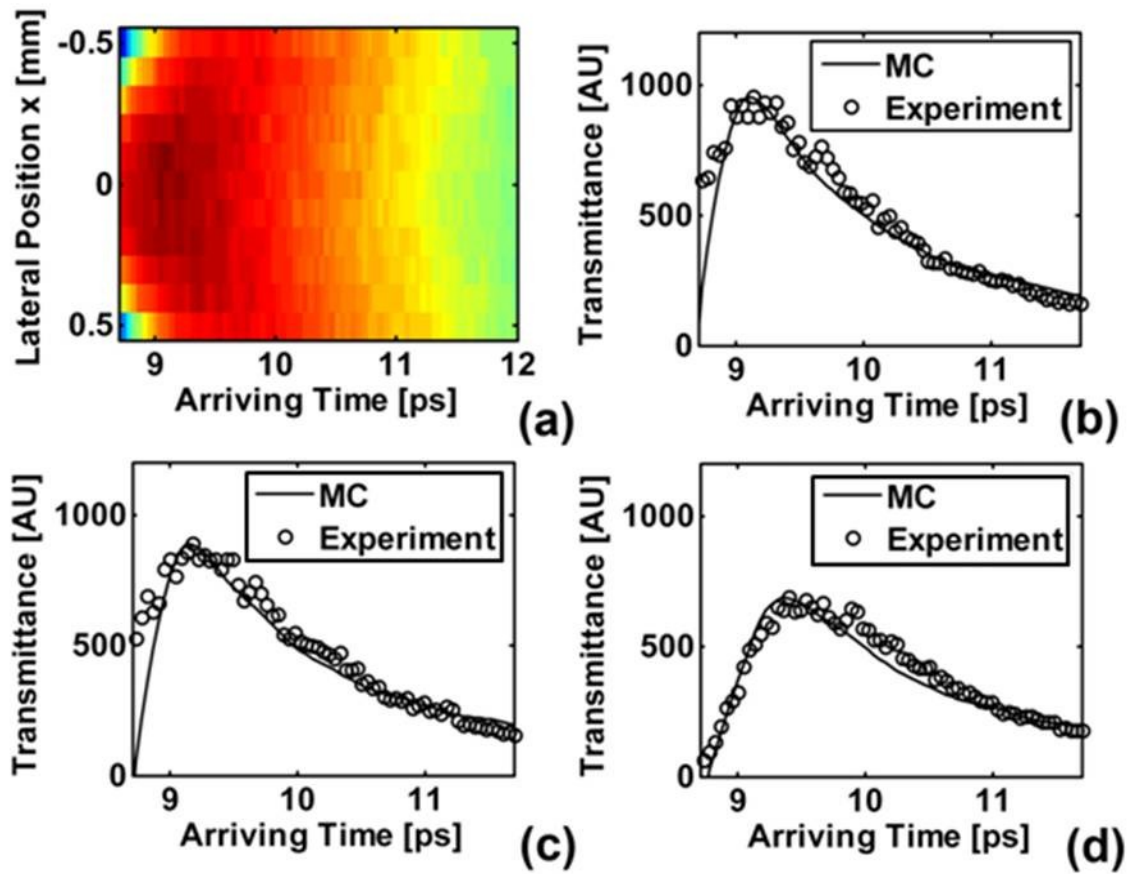
Figure 4.2 Comparison between temporal profiles of light measured in optical CCT and predicted by Monte Carlo simulation. (a) Experimental measurements obtained at source-detector pairs with lateral shift x=-0.5 mm to 0.5 mm. Experimental measurements at (b) x=0 mm, (c) x=0.2 mm and (d) x=0.4 mm are compared with the predictions from the simulation. MC: Monte Carlo simulation.

4.4.2   Imaging Absorbing Objects Using Optical CCT

We then demonstrated imaging absorbing objects in highly scattering medium by optical

CCT experimentally.

68

A 100-μm hair fiber was immersed parallel to the y-axis inside the tissue-mimicking medium described above. Three tomographic images were obtained when this hair fiber was placed at three different depths with a 0.5-mm separation. For each position, data were collected at 11×11 source-detector pairs, which covered a 1-mm range along the x-axis. Figure 4.3(a) shows the three reconstructed optical CCT images of the hair fiber thresholded at 50% of the peak value in the image. The hair fiber was clearly identified at all three expected positions. The full width at half maximum (FWHM) of the imaged hair is 200 μm along the z-direction and 180 μm along the x-direction, both of which are ~100 μm wider than the actual diameter of the hair fiber. Under the assumption of a linear system, the spatial resolution of our optical CCT system is estimated to be ~100 μm. This resolution maintains well throughout the whole phantom. The thickness of the phantom is equivalent to ~30 scattering mean-free-paths, which is much thicker than the maximal penetration depth of OCT (~10 scattering mean-free-paths).

Also, Figure 4.3(b) shows the reconstructed image of two hair fibers in the same scattering medium, with a 1.3 mm separation in both the *x* and *z* directions. Transmitted light was measured at 21×21 source-detector pairs, which covered a 2-mm range along the x-axis. This demonstrates optical CCT is capable of mapping multiple absorption perturbations simultaneously.

69
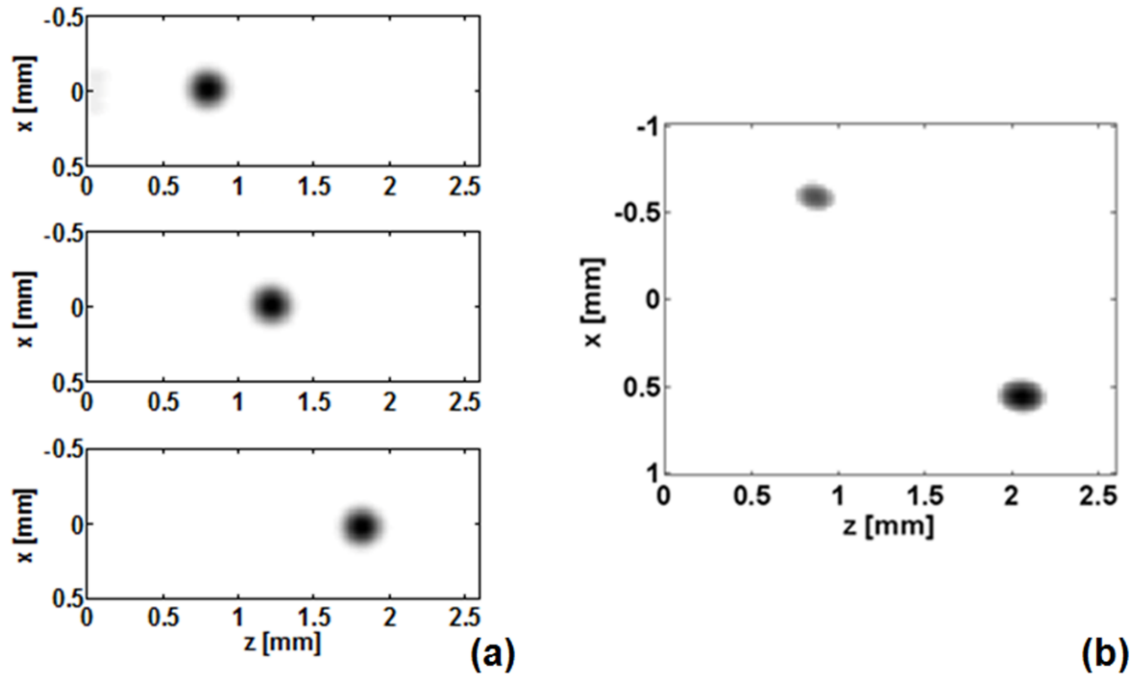
Figure 4.3   Optical CCT images of absorbing objects in highly scattering tissue-mimicking phantom. (a) Reconstructed images of a 100-μm hair fiber at three different depths with 0.5-mm separation. (b) Reconstructed image of two hair fibers with 1.3-mm separation along both the x and z directions.

4.5   Conclusion

In a brief summary, we proposed and demonstrated a new time-resolved optical tomography, optical CCT. Optical CCT measures the reemitted light from tissue with a superior temporal resolution by a low-coherence interferometer. By using a model-based reconstruction algorithm, optical CCT makes use of both singly and multiply scattered photons. As a result, optical CCT can work in both the ballistic and quasi-diffusive regime. We experimentally proved that our current optical CCT system penetrated deeper than traditional OCT, and maintains consistent imaging quality through the whole

70

imaging depth. Furthermore, optical CCT is sensitive to optical absorption, thus could provide information about the molecular content of tissue.

Spectroscopic OCT has been proposed to extract absorption contrast at the cost of spatial resolution by exploiting spectral features of absorption [116]. However, this method is susceptible to the spectral variation of the scattering coefficient μ_s, which sometimes dominates spectral features of optical absorption. Also, it is also unable to detect absorbers whose absorption coefficient μ_a does not change much in the source bandwidth. Optical CCT doesn't rely on spectroscopic measurement, thus can avoid these problems.

Previous development of pure optical imaging methods for the quasi-diffusive regime is limited to laminar optical tomography [117, 118], which uses continuous-wave measurements. The image quality relies on proper regularization, and decays with depth. Since time-resolved measurements are adopted in optical CCT, the inverse problem is less ill-posed and the reconstruction is more robust.

Diffuse optical tomography (DOT) measures diffusive photons using other methods, and provides maps of tissues' optical properties through model-based reconstruction from measurements at a large number of source-detection pairs. It can image a few centimeters into tissue using near-infrared light. However, the spatial resolution achieved is relatively poor, typically on the order of millimeters (1/5 of the imaged depth), due to the nature of diffusion. Time-domain DOT measures the time-resolved reemission of light from a medium in response. It is expected to outperform continuous-wave and frequency-domain versions, since it carries information of the whole spectrum simultaneously. Traditionally, time-resolved profile of light was measured by expensive sophisticated

71

high-sensitivity detection systems, such as a streak camera [119] and a time-correlated single-photon counting system [120] with ps-order resolution. However, the slow frame-rate and the high cost limited their application. Recently, time-gated optical image intensifier [121] has been utilized to develop fast parallel time-resolved DOT. However, the gate width is ~200 ps, corresponding to a pathlength as long as 6 cm in air. A finer temporal resolution is preferred to resolve small lesions in tissue. Using a low-coherence interferometer, our current CCT system could measure light with a superior temporal resolution of 56 fs at relatively low cost, and achieves a sub-mm resolution better than DOT. Optical CCT could potentially bridge the gap between OCT and DOT, which means it can image deeper than OCT with a resolving power better than that of DOT.

Chapter 5　Conclusion and Future Directions

In this study, built on the spirits of photoacoustic imaging and optical coherence tomography, I developed three novel optical imaging techniques: photoacoustic reporter gene imaging, integrated photoacoustic and optical coherence microscopy (iPOM), and optical coherence computed tomography (optical CCT). In this final chapter, I want to discuss current challenges that we are facing in advancing these techniques, and suggest several future directions.

We believe the combination of photoacoustic imaging and chromogenic reporter gene system could result in a new paradigm for molecular imaging. However, the *lacZ*/X-gal reporter strategy used in this study has its limitations. The cleavage of X-gal can occasionally cause skin irritation and the *in vivo* dynamics of the reaction is poorly understood. Currently, X-gal was introduced locally. After systemic injection through tail vein, the blue product did not seem to accumulate at a detectable concentration. Also, the blue product was found to slowly diffuse out from *lacZ*-marked tumor cells into surrounding tissue with time. Hence we are looking for collaborative effort from the biochemical society to design a better reporter probe to replace X-gal to report the *lacZ* expression *in vivo*. First, after reaction with β-galactosidase, the cleaved product of this probe should have a large absorption cross-section in the red or near-infrared part of optical spectrum. Second, it should be able to be efficiently delivered to targeted tissue following a systemic introduction. Finally, the final product is preferred to be trapped inside cells that expressing *lacZ*. More importantly, we propose to explore new chromogenic reporter gene systems, especially those doesn't require the introduction of

reporter probes. Considering the vast array of colors in the natural world, this may prove to be a fruitful direction of research that could significantly impact the field of molecular imaging.

In terms of iPOM, the next technical advance will be integrating the complementary functional imaging capabilities of PAI and OCT into the system. PAI could quantify the local hemoglobin concentration and blood oxygenation, and relative changes in temperature, while OCT is good at estimating local blood flow. As a result, iPOM not only can provide all these important established functional parameters, but also is potentially able to provide new functional biomarkers of diseases, such as the local oxygen consumption rate. Also, iPOM could be performed at the video rate by adopting a laser with higher pulse repetition rate, and delivering light through a photonic crystal fiber that can deliver higher energy laser pulse. Finally, I believe iPOM will not only find broad applications in laboratorial studies of microcirculation, neuroscience and tissue engineering, but also experience a rapid clinical translation to help diagnose and treat dermatological and ophthalmological diseases.

To advance optical CCT, a fast forward model for photon migration in the pre-diffusive is highly desirable. Due to the statistical nature of the Monte Carlo method, the current forward calculation is extremely computation intensive. What's more, the linear equation in Equation (4.2) will not work when perturbations are large. In that case, a non-linear image reconstruction problem needs to be solved the RTE without the linearization iteratively. Recently, motivated by the development of time-resolved optical imaging techniques, researchers have started to develop fast numerical solutions for solving the

full transient RTE based on the discrete transfer method, the discrete ordinates method and finite volume method [122]. However, further studies are needed to clarify their applications in the content of biomedical optical imaging, especially for the quasi-diffusive regime. Their accuracy need to be tested against the Monte Carlo method, a well-accepted golden standard. Also, it should be possible to reconstruct a map of tissues' scattering coefficient and phase function following similar procedures as presented in this study. In addition, many biomedical applications require us to further implement optical CCT in reflection mode. The major obstacle there is that the strong specular reflection from the air-tissue interface will dominate the light scattered from the inside of the tissue, and raises the noise floor in measurements. We may potentially solve the problem by apply proper couplant on the tissue surface, or reject the strong specular reflection by a cross-polarization technique. Finally, I expect that optical CCT can be scaled up to image thicker tissues (>1 cm) by relaxing the temporal resolution, because the number of photons detected at each time point increases by extending time gate. Of course, this will likely be done at the cost of spatial resolution. Detection of light after penetrating 1.5-cm chicken tissue was previously reported by relaxing the time gate to 900 fs [123].

Appendix A   The Speckle-free Nature of Photoacoustic Imaging[§]

A.1   Introduction

Speckle has been considered ubiquitous in all coherent imaging modalities, such as laser imagery [124, 125] , ultrasonography [126, 127] , synthetic aperture radar [128], and optical coherence tomography [129]. Fully developed speckle is formed by the interference among partial waves, either scattered from randomly distributed scatterers or reflected from a rough surface, whose phases are completely randomized over 2π. The speckle pattern generally has a high-contrast, fine-scale granular appearance, which does not correspond to the real structure of the sample. Although useful in certain applications, such as optical speckle imaging and ultrasound tissue characterization, speckle reduces both the effective spatial resolution and the detectability of small lesions, and thus deteriorates the image quality significantly. Many efforts have been made to mitigate this undesirable deterioration; however, speckle can be only partially reduced and only at the cost of system complexity, imaging time, or spatial resolution.

A long-standing conundrum is why photoacoustic imaging (PAI) possesses the unique ability to produce images devoid of speckle artifacts while all other coherent imaging

---

[§] Reprinted with permission from Z. Guo*, L. Li*, and L. V. Wang, "On the speckle-free nature of photoacoustic tomography," *Medical Physics* 36, 4084–4088 (2009). (*These Authors contributed equally to this work.)

technologies do not. We found that this feature of PAI results directly from the optical absorption contrast. All optical absorbers expand on laser excitation, and therefore all initial photoacoustic pressure rises are positive, which engenders strong correlations among the photoacoustic waves from the absorbers. As a result, prominent boundaries always build up in photoacoustic images and suppress the interior speckle. This analysis was validated by simulations based on an experimental

A.2   Three Theoretical Explanations

When researchers analyze the speckle statistics in ultrasound imaging, a scattering structure is usually modeled as a collection of randomly distributed sub-resolution scatterers. The ultrasonic waves scattered from these scatterers interfere with each other, and a speckle results. Owing to the structural continuity, the scattered waves usually possess either positive or negative polarity. Similarly, in PAI, an optically absorbing structure can be modeled as a collection of randomly distributed sub-resolution absorbers. The absorbers can vary in dimension widely, from hemoglobin molecules to red blood cells, as long as they are much smaller than the spatial resolution. The axial resolution of the 5-MHz PAI system, limited by the transducer bandwidth, is ~144 μm. The lateral resolution, determined by the width of the focal spot, is ~560 μm. Because an average adult has ~5 million red blood cells (~7.4–9.4 μm in diameter and ~1.6–2.0 μm in thickness) per microliter of blood, the ultrasonic transducer may receive photoacoustic waves from ~5.8×   red blood cells within a resolution cell. The photoacoustic signals emitted from these absorbers interfere with each other. Curiously, investigators have

77

noticed that photoacoustic methods, despite their coherent nature, produce images devoid of speckle artifacts. We found that this salient feature is a direct result of the absorption contrast in PAI.

As the first explanation of the speckle-free nature of PAI, we compare a pulse-echo ultrasound imaging system with the 5-MHz reflection-mode PAI system. Both systems can be described by the same linear model. For a fair comparison without loss of generality, the same spatial-temporal system impulse response $h(\bar{r}, t)$ is assumed for both systems. In reality, $h(\bar{r}, t)$ in pulse-echo ultrasonography represents a round trip response, while $h(\bar{r}, t)$ in PAI represents only one way.

Figure A.1 shows that a focused ultrasonic transducer detects A-scan signals from a slab of tissue. The tissue slab is modeled as a collection of randomly distributed particles (red dots), which can be either acoustic scatterers in ultrasound imaging or optical absorbers in PAI. For simplicity, we consider the particles as point targets because they are small relative to the spatial resolution. In the ultrasonic A-scan, the received signals from the individual scatterers may either maintain (red solid curves) or flip (blue dotted curves) the polarity of $h(\bar{r}, t)$, because the acoustic impedance of the scatterers may be either lower or higher than the surrounding medium. The photoacoustic A-scan from the absorbers of the same geometry is also plotted. Because all initial pressure rises are positive, all received photoacoustic waves uphold the polarity of $h(\bar{r}, t)$, which is the major difference between PAI and ultrasound imaging. The A-scan signals, plotted in green dashed lines, result from the interference among the signals from the individual

78

particles. In the middle segment of the A-scan signals in both imaging modalities, we observe random fluctuations, because of the cancellation among the positive and negative parts of $h(\vec{r}, t)$. Further, the mean of the amplitudes of the fluctuations are zero because $h(\vec{r}, t)$ does not contain a DC component (in the cases when very wideband acoustic sensors that can detect DC component are employed in PAI, we expect to see not only the boundary buildups, but also the baselines inside the object.). Near both the front and back boundaries, however, prominent boundary signals are observed in the photoacoustic A-scan, because of the constructive interferences. As a result, the random fluctuations in the middle are suppressed by the boundary signals, which we found to be the dominant features in photoacoustic images. By contrast, the boundary signals in ultrasound images do not stand out because of the existence of both scattering polarities. Therefore, speckle appears ubiquitously in ultrasonic A-scans.
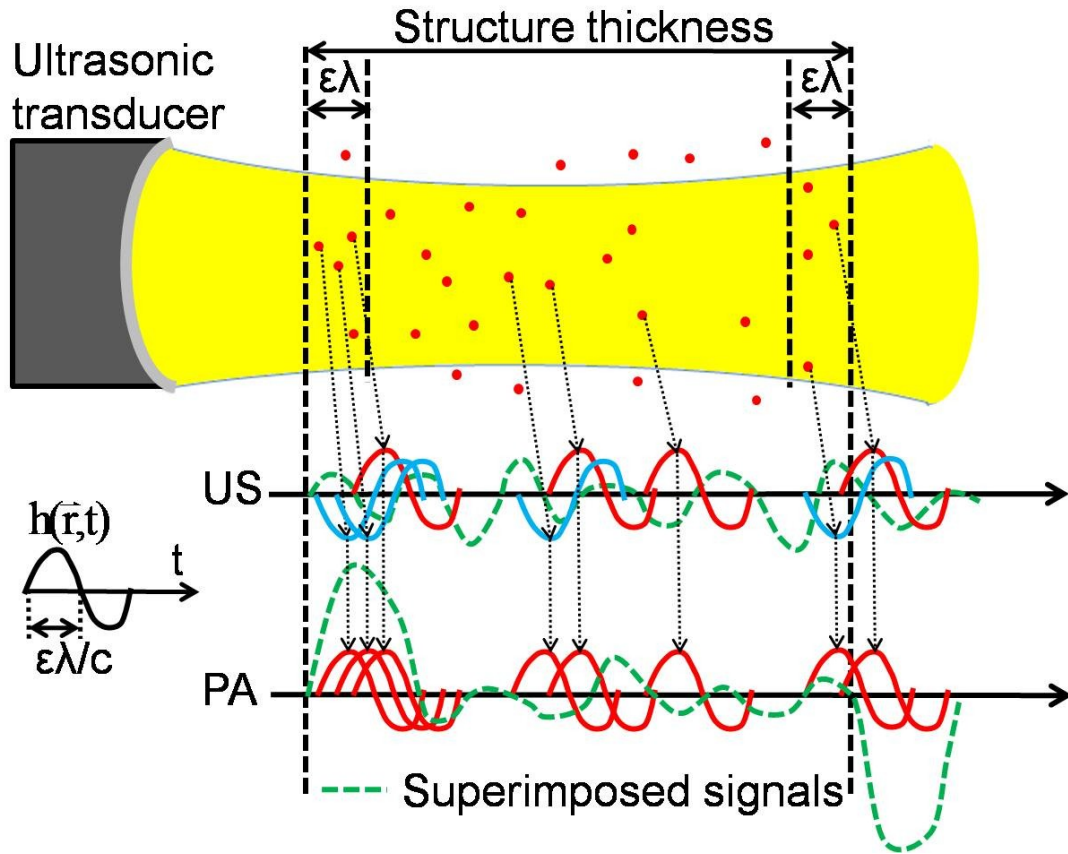
Figure A.1 Comparison of pulse-echo ultrasound imaging and reflection-mode PAI. A focused ultrasonic transducer records the A-scan signal from a slab. $\varepsilon\lambda$: a fraction of the central acoustic wavelength λ; c: speed of ultrasound. PA: Photoacoustic; US: Ultrasound.

As the second explanation, the classic speckle theory, which usually models only monochromatic waves, is invoked. As stated above, the fully developed speckle is formed by the interference of coherent waves with completely randomized phases. Two components contribute to the phase difference between waves: the initial phase and the phase delay. When profiling the central part of the structure in both photoacoustic and ultrasound imaging, we always receive acoustic waves from particles with completely

randomized phases, which result from phase-delay variations. However, particles close to the boundaries send out waves that reach the transducer with approximately equal phase delays. Here, the initial phase plays a key role. As the initial photoacoustic pressure rises are always positive, the emitted photoacoustic waves add constructively to manifest the boundaries. By contrast, the scattered ultrasonic waves can take on both positive and negative initial phases. Hence, no boundary buildups are observed.

As the third explanation, we analyze the condition for building up boundaries in all coherent imaging modalities and compare the strengths of the boundaries and of the interior speckle in PAI quantitatively. Assume that a total of n particles (absorber or scatterer) are statistically uniformly distributed at positions $\vec{r}_1, \vec{r}_2 \cdots\cdots \vec{r}_n$. We use random process $a_i(t)$ to denote the particle impulse response, which accounts for the properties of a single particle. Because PAI is based on the optical absorption contrast, $a_i(t)$ depends on the optical absorption, shape, and size of the absorber [130]. As an absorber quickly expands on laser excitation, a strong positive initial pressure is always generated. Consequently, the early part of $a_i(t)$ is always positive. In ultrasound imaging, as a typical scattering-based imaging modality, $a_i(t)$ is related to the acoustic properties (density and compressibility), shape, and size of the scatterer [131]. In reality, the shape of $a_i(t)$ is relatively random. The amplitude of an A-scan can be written as

$$A(t) = \sum_{i=1}^{n} a_i(t) \underset{t}{*} h(\vec{r}_i, t - |\vec{r}_i|/c) \qquad \text{(A. 1)}$$

81

where $\overset{*}{t}$ denotes convolution in the time domain, and c denotes the propagation velocity of the ultrasonic wave. When Eq ((A. 1) is applied to ultrasound imaging, round trip delays and multiple scattering are neglected because they are not key factors in our discussions. The instantaneous power of an A-scan is $P(t) = A^2(t)$, and the ensemble average of $P(t)$ becomes

$$\langle P(t) \rangle = \rho_0 \int_V \left\langle \left\langle \left(a_i(t) \overset{*}{t} h(\bar{r}, t - |\bar{r}|/c) \right)^2 \right\rangle \right\rangle_i d\bar{r}^3 + \rho_0^2 \left\langle b_i(t) b_j(t) \right\rangle_{i \neq j} \qquad \text{(A. 2)}$$

where $b_i(t) = \langle a_i(t) \rangle \overset{*}{t} \int_V h(\bar{r}, t - |\bar{r}|/c) d\bar{r}^3$, ρ_0 is the particle density, V is the structure volume, $\langle \ \rangle_i$ is averaging over all n particles, and $\langle \ \rangle_{i \neq j}$ is averaging over all particle pairs.

The first term in Eq. ((A. 2) is the sum of the powers of the waves generated from all particles. Therefore, it is called the uncorrelated contribution to the total power. It represents the power of the random fluctuations—speckle, which is shared in both imaging modalities. Speckle in ultrasound imaging has been widely used for tissue characterization [132].

The second term in Eq. (2) is responsible for the prominent boundary features in photoacoustic images. Because this term represents the correlations among the particles, it is responsible for the correlated contribution to the total power. First, the correlated power appears only as boundary features, because $\int_V h(\bar{r}, t - |\bar{r}|/c) d\bar{r}^3$ is always zero inside the structure. Second, the correlated power exists in photoacoustic images but

usually disappears in ultrasound images. As stated above, $a_i(t)$ in PAI always starts with a positive value, which produces strong correlations among the absorbers. After averaging over all particle pairs, the correlated power shows up as strong boundary features in PAI. In ultrasound imaging, however, the polarity of $a_i(t)$ is relatively random. After averaging, the correlated power usually becomes negligible.

Eq. ((A. 2) can be further simplified by assuming the particles to be point targets. The photoacoustic wave from each point target excited by a delta laser pulse becomes $a_i(t) = a_i \delta'(t)$, where each a_i is a random variable with a positive mean. In ultrasound imaging, researchers usually assume $a_i(t) = a_i \delta(t)$, where each a_i is a zero mean random variable [133] because the scattered signal is due to fluctuations in acoustic properties relative to the mean. By substituting $a_i(t) = a_i \delta'(t)$ or $a_i(t) = a_i \delta(t)$ into Eq. ((A. 2), we have

$$\langle P(t) \rangle = \left(\sigma_a^2 + a^2 \right) \rho_0 \int_V \left(\tilde{h}(\bar{r}, t - |\bar{r}| / c) \right)^2 d\bar{r}^3 + a^2 \rho_0^2 \left(\int_V \tilde{h}(\bar{r}, t - |\bar{r}| / c) d\bar{r}^3 \right)^2 \qquad \text{(A. 3)}$$

Since integral with $\delta'(t)$ denotes differentiation with respect to time, we have $\tilde{h}(\bar{r}, t) = h'(\bar{r}, t)$ in PAI and $\tilde{h}(\bar{r}, t) = h(\bar{r}, t)$ in ultrasound imaging. Here a and σ_a^2 are the mean and variance of a_i, respectively.

From Eq. ((A. 3), we can quantify the visibility of the interior speckle in PAI, which is defined as the ratio of the square root of the average speckle power to the magnitude of boundary features, which are composed of both uncorrelated and correlated powers. The

uncorrelated power is proportional to ρ_0, while the correlated power is proportional to ρ_0^2. When ρ_0 is sufficiently large, the correlated power is much stronger than the uncorrelated power, and the speckle visibility in PAI is approximately inversely proportional to $\sqrt{\rho_0}$. In this case, the correlated power dominates the photoacoustic image. From Eq. ((A. 3), we also note that the visibility of speckle in PAI does not depend on the particle absorbing strength, because both the correlated and uncorrelated powers are proportional to a^2. In ultrasound imaging, the second term in Eq. ((A. 2) and Eq. ((A. 3) equals zero, and the correlated contribution is usually negligible. Therefore, the speckle visibility is independent of the scatterer density. The uncorrelated power dominates in ultrasound imaging and all other scattering-based coherent imaging modalities.

A.3   Simulation of a Photoacoustic Imaging System

We use simulation to further illustrate our analysis. Our numerical phantom contains a 5-mm thick tissue structure, whose center is located 5 mm away from the transducer surface. It is composed of a large number of absorbers randomly distributed between 2.5 mm and 7.5 mm along the ultrasonic axis. The transducer is assumed to have 5-MHz central frequency with 100% bandwidth. Figure A.2 compares the photoacoustic profile with the ultrasound profile, where the exact boundary positions are marked as vertical dotted lines. The envelopes represent the magnitude of absorption or scattering.
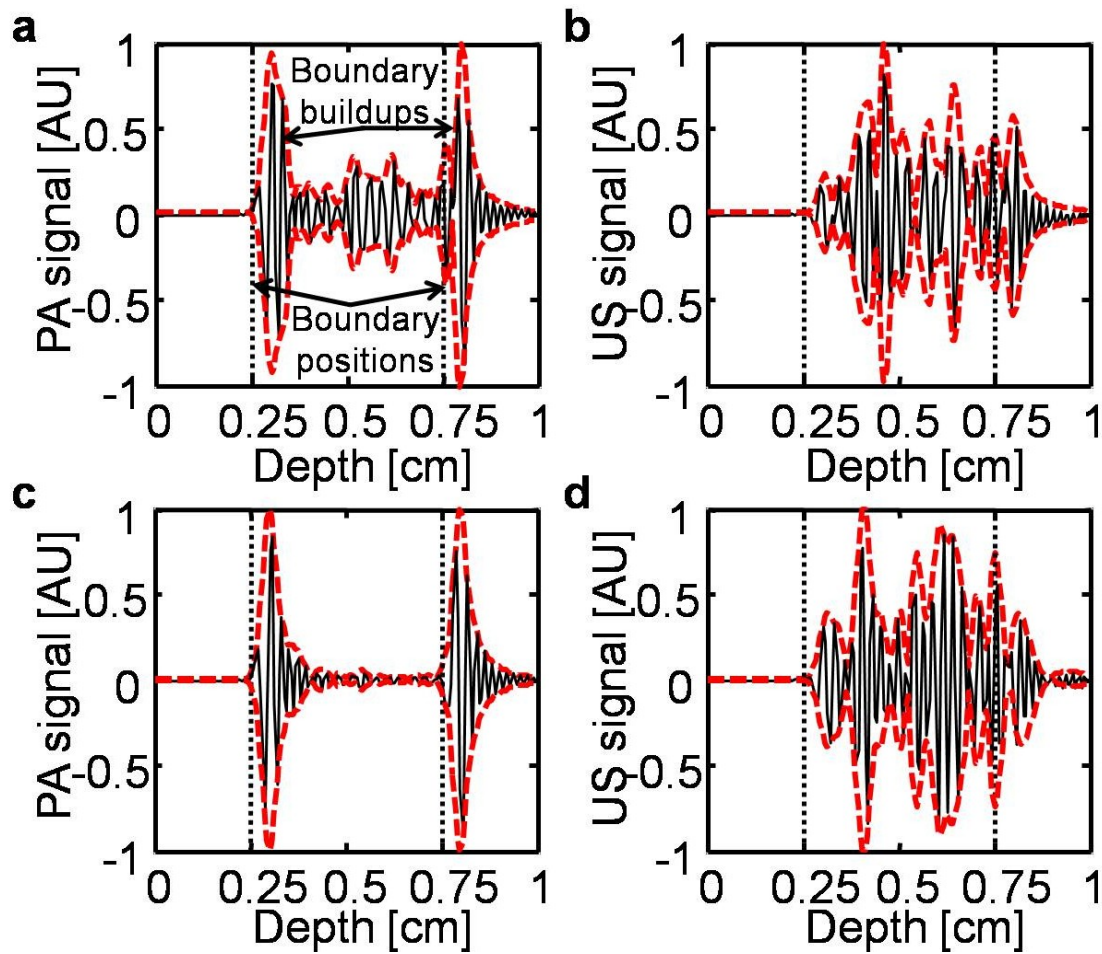
Figure A.2 Simulated depth profiles of a slab. (a) PAI, absorber density: 1,000/λ. (b) Ultrasound imaging, scatterer density: 1,000/λ. (c) PAI, absorber density: 100,000/λ. (d) Ultrasound imaging, scatterer density: 100,000/λ. λ: the acoustic wavelength of 5-MHz ultrasound. PA: Photoacoustic; US: Ultrasound.

Between Figure A.2 (a) and (b), the object has the same particle density. In the photoacoustic A-scan [Figure A.2(a)], we notice two prominent semi-deterministic boundaries, which dominate the random speckle fluctuations in between. The separation between either maximum profile position and the corresponding boundary position is a fraction of the center ultrasonic wavelength. In the ultrasonic A-scan [Figure A.2(b)], the

speckle fluctuations spread across the entire imaged object, and no outstanding boundaries are observed.
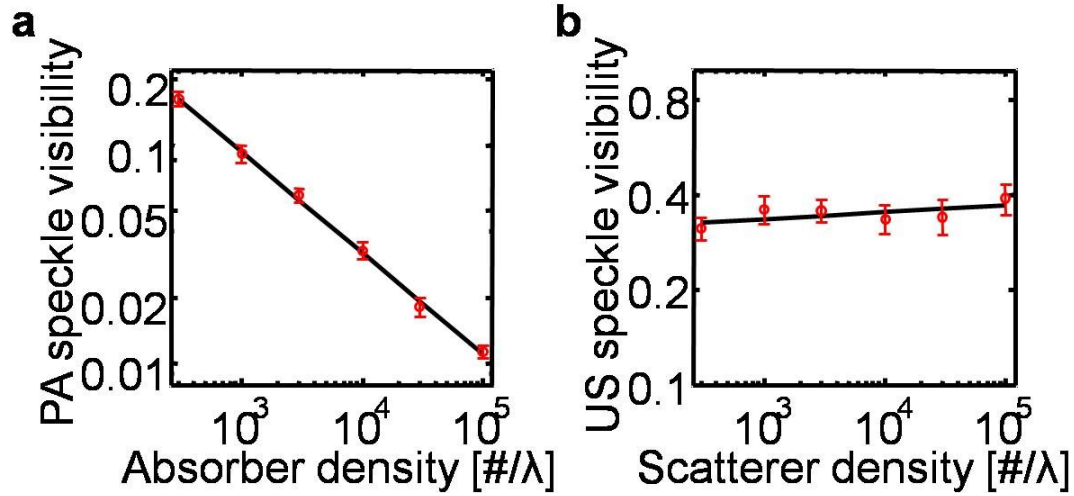
Figure A.3   Relationship between the speckle visibility in photoacoustic/ultrasound imaging and the absorber/scatterer density. (a) PAI; (b) Ultrasound imaging. Error bars: standard errors of the means (circles) based on 10 realizations of particle distributions; solid lines: linear fits. PA: Photoacoustic; US: Ultrasound.

In PAI, the visibility of the interior speckle was also found to decrease with increase in absorber density, as demonstrated in Figure A.2 (a) and (c) and further quantified in Figure A.3(a). The linear fit between the logarithm of the speckle visibility and the absorber density has a slope of –0.479±0.003, which is close to the inverse square-root dependence as predicted above. By contrast, the speckle visibility stays approximately constant in the ultrasound images, as illustrated in Figure A.2(b) and (d) and further quantified in Figure A.3(b). In both Figure A.2(a) and (c), each middle segment—between the two outermost minima of the profile within the two maxima—proves to be a fully developed speckle, because the magnitude of the photoacoustic signal follows the

86

Rayleigh distribution and the intensity follows the exponential distribution. Therefore, the simulation confirms the aforementioned explanations.

In Figure A.4(a) and (b), we present simulated photoacoustic and ultrasonic cross-sectional images (B-scan) of a round tumor, where the exact boundaries of the tumors are plotted as dashed lines. The ultrasound spatial-temporal response of the 5-MHz focused ultrasonic transducer is calculated by the Field II program [134]. We first simulate the case when the absorbing or scattering strength of the particles in the tumor area is 10 times that of the background particles. For a large tumor with a diameter of 2 mm, strong signals at its top and bottom boundaries are observed in the photoacoustic B-scan [Figure A.4(a)]. The side boundaries are missing due to the limited view of the linear detection geometry. Figure A.4(b) shows the corresponding ultrasonic B-scan image, where speckle artifacts prevail. The higher scattering strength of the tumor induces a stronger speckle in the tumor area, which suppresses the background speckle. In reality, a 10:1 scattering strength contrast is usually unavailable in ultrasound imaging. Therefore, the background speckle may be more prominent.

In Figure A.4(c) and (d), respectively, the photoacoustic and ultrasonic B-scans of a sub-resolution-sized tumor with a diameter of 100 μm are shown. In Fig. 4c, the small tumor appears in the photoacoustic B-scan image as a solid area without distinct front and back boundaries. In Figure A.4(d), the tumor cannot be identified in the ultrasonic B-scan image. We also simulated the case when the particle density is higher in the tumor area. As expected, the interior speckle is further suppressed in the photoacoustic image, whereas the visibility of speckle remains unchanged in the ultrasound image.

87
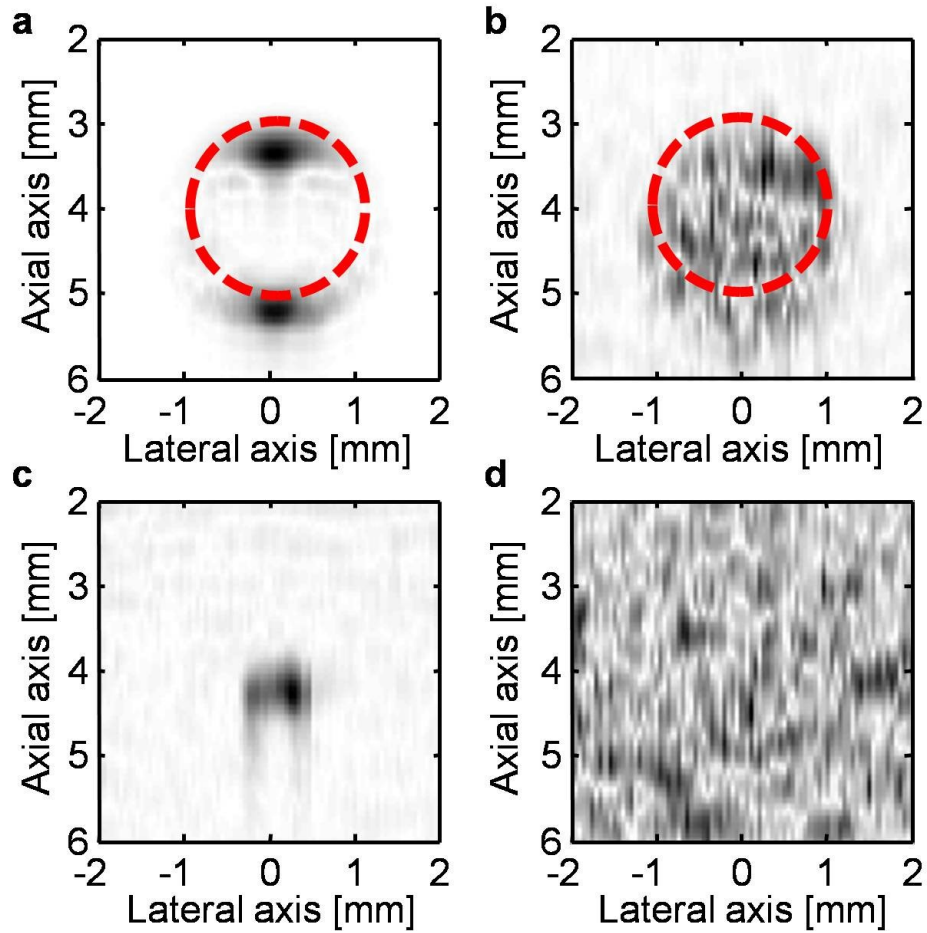
Figure A.4 Simulated cross-sectional photoacoustic and ultrasonic images of round tumors. Photoacoustic/ultrasonic B-scans of tumors with 2 mm diameter (a/b) and 100 μm diameter (c/d). Absorber/scatterer density: 5 million/μL. Absorbing/scattering strength contrast: 10:1.

A.4   Discussion and Conclusion

We should note that the correlated power can also exist in ultrasound imaging in rare cases. For example, the observation of correlated power at scatterer concentration gradients (boundaries) in ultrasonic A-scans of a sponge slab was reported [135]. If the shape, size and acoustic properties of the scatterers within the structure volume are

88

similar, the correlation among the particle impulse responses becomes strong. As a result, the correlated power may show up at the boundaries. However, this assumption usually does not hold in real human tissue, and hence no boundary buildup occurs.

We conclude that speckle artifacts in PAI are suppressed by prominent boundary buildups. The initial all-positive photoacoustic pressure rises provide strong correlation among the absorbers, which gives rise to strong boundary buildups. While images from ultrasound imaging and all other scattering-based imaging modalities are dominated by uncorrelated power, photoacoustic images are dominated by correlated power.

References

1.   L. V. Wang, and H. I. Wu, *Biomedical Optics: Principles and Imaging* (Wiley, New Jersy, 2007).

2.   M. Minsky, "Memoir on Inventing the Confocal Scanning Microscope," Scanning **10**, 128-138 (1988).

3.   W. Denk, J. H. Strickler, and W. W. Webb, "Two-photon laser scanning fluorescence microscopy," Science **248**, 73-76 (1990).

4.   A. Zumbusch, G. R. Holtom, and X. S. Xie, "Three-Dimensional Vibrational Imaging by Coherent Anti-Stokes Raman Scattering," Physical Review Letters **82**, 4142 (1999).

5.   S. W. Hell, "Far-field optical nanoscopy," Science **316**, 1153-1158 (2007).

6.   S. W. Hell, and J. Wichmann, "Breaking the Diffraction Resolution Limit by Stimulated-Emission - Stimulated-Emission-Depletion Fluorescence Microscopy," Optics Letters **19**, 780-782 (1994).

7.   H. Shroff, C. G. Galbraith, J. A. Galbraith, and E. Betzig, "Live-cell photoactivated localization microscopy of nanoscale adhesion dynamics," Nature Methods **5**, 417-423 (2008).

8.   M. J. Rust, M. Bates, and X. W. Zhuang, "Sub-diffraction-limit imaging by stochastic optical reconstruction microscopy (STORM)," Nature Methods **3**, 793-795 (2006).

9.   A. Yodh, and B. Chance, "Spectroscopy and Imaging with Diffusing Light," Physics Today **48**, 34-40 (1995).

10.   A. G. Bell, "On the production and reproduction of sound by light," Am. J. Sci. **20**, 305-324 (1880).

11.   L. V. Wang, "Ultrasound-mediated biophotonic imaging: A review of acousto-optical tomography and photo-acoustic tomography," Disease Markers **19**, 123-138 (2003).

12.   V. Ntziachristos, J. Ripoll, L. V. Wang, and R. Weissleder, "Looking and listening to light: the evolution of whole-body photonic imaging," Nature Biotechnology **23**, 313-320 (2005).

13.   M. Xu, and L. V. Wang, "Photoacoustic imaging in biomedicine," Review of Scientific Instruments **77**, - (2006).

14.   L. V. Wang, "Tutorial on photoacoustic microscopy and computed tomography," Ieee Journal of Selected Topics in Quantum Electronics **14**, 171-179 (2008).

15.   L. V. Wang, "Multiscale photoacoustic microscopy and computed tomography," Nature Photonics **3**, 503-509 (2009).

16.   C. Li, and L. V. Wang, "Photoacoustic tomography and sensing in biomedicine," Physics in Medicine and Biology **54**, R59-R97 (2009).

17.   X. Wang, Y. Pang, G. Ku, X. Xie, G. Stoica, and L. V. Wang, "Noninvasive laser-induced photoacoustic tomography for structural and functional in vivo imaging of the brain," Nature Biotechnology **21**, 803-806 (2003).

18.   H. F. Zhang, K. Maslov, G. Stoica, and L. V. Wang, "Functional photoacoustic microscopy for high-resolution and noninvasive in vivo imaging," Nature Biotechnology **24**, 848-851 (2006).

19.   K. Maslov, H. F. Zhang, S. Hu, and L. V. Wang, "Optical-resolution photoacoustic microscopy for in vivo imaging of single capillaries," Optics Letters **33**, 929-931 (2008).

20.   J. T. Oh, M. Li, H. F. Zhang, K. Maslov, G. Stoica, and L. V. Wang, "Three-dimensional imaging of skin melanoma in vivo by dual-wavelength photoacoustic microscopy," Journal of Biomedical Optics **11**, 034032 (2006).

21.   Z. Xu, C. Li, and L. V. Wang, "Photoacoustic tomography of water in phantoms and tissue," Journal of Biomedical Optics **15**, 036019 (2010).

22.   H. F. Zhang, K. Maslov, M. Sivaramakrishnan, G. Stoica, and L. V. Wang, "Imaging of hemoglobin oxygen saturation variations in single vessels in vivo using photoacoustic microscopy," Applied Physics Letters **90**, 053901 (2007).

23.   L. Li, R. J. Zemp, G. Lungu, G. Stoica, and L. V. Wang, "Photoacoustic imaging of lacZ gene expression in vivo," Journal of Biomedical Optics **12**, 020504 (2007).

24.   L. Li, H. F. Zhang, R. J. Zemp, and L. V. Wang, "Simultaneous imaging of a lacZ-marked tumor and microvasculature morphology in vivo by dual-wavelength photoacoustic microscopy," Journal of Innovative Optical Health Sciences **1**, 207-215 (2008).

25.   M. Li, J. Oh, X. Xie, G. Ku, W. Wang, C. Li, G. Lungu, G. Stoica, and L. V. Wang, "Simultaneous molecular and hypoxia imaging of brain tumors in vivo using spectroscopic photoacoustic tomography," Proceedings of the IEEE **96**, 481-489 (2008).

26.   P. C. Li, C. R. C. Wang, D. B. Shieh, C. W. Wei, C. K. Liao, C. Poe, S. Jhan, A. A. Ding, and Y. N. Wu, "In vivo Photoacoustic Molecular Imaging with Simultaneous Multiple Selective Targeting Using Antibody-Conjugated Gold Nanorods," Optics Express **16**, 18605-18615 (2008).

91

27.   G. Ku, K. Maslov, L. Li, and L. V. Wang, "Photoacoustic microscopy with 2-μm transverse resolution," Journal of Biomedical Optics **15**, 021302 (2010).

28.   C. Zhang, K. Maslov, and L. V. Wang, "Subwavelength-resolution label-free photoacoustic microscopy of optical absorption in vivo," Optics Letters **35**, 3195-3197 (2010).

29.   S. Hu, K. Maslov, and L. V. Wang, "Noninvasive label-free imaging of microhemodynamics by optical-resolution photoacoustic microscopy," Optics Express **17**, 7688-7693 (2009).

30.   K. Maslov, G. Stoica, and L. V. Wang, "In vivo dark-field reflection-mode photoacoustic microscopy," Optics Letters **30**, 625-627 (2005).

31.   H. F. Zhang, K. Maslov, and L. V. Wang, "In vivo imaging of subcutaneous structures using functional photoacoustic microscopy," Nature Protocols **2**, 797-804 (2007).

32.   E. W. Stein, K. Maslov, and L. V. Wang, "Noninvasive, in vivo imaging of the mouse brain using photoacoustic microscopy," Journal of Applied Physics **105**, 102027 (2009).

33.   G. Ku, and L. V. Wang, "Deeply penetrating photoacoustic tomography in biological tissues enhanced with an optical contrast agent," Optics Letters **30**, 507-509 (2005).

34.   S. A. Ermilov, T. Khamapirad, A. Conjusteau, M. H. Leonard, R. Lacewell, K. Mehta, T. Miller, and A. A. Oraevsky, "Laser optoacoustic imaging system for detection of breast cancer," Journal of Biomedical Optics **14**, 024007 (2009).

35.   X. D. Wang, D. L. Chamberland, and G. H. Xi, "Noninvasive reflection mode photoacoustic imaging through infant skull toward imaging of neonatal brains," Journal of Neuroscience Methods **168**, 412-421 (2008).

36.   T. N. Erpelding, C. Kim, M. Pramanik, L. Jankovic, K. Maslov, Z. Guo, J. A. Margenthaler, M. D. Pashley, and L. V. Wang, "Sentinel Lymph Nodes in the Rat: Noninvasive Photoacoustic and US Imaging with a Clinical US System," Radiology **256**, 102-110 (2010).

37.   D. Huang, E. A. Swanson, C. P. Lin, J. S. Schuman, W. G. Stinson, W. Chang, M. R. Hee, T. Flotte, K. Gregory, C. A. Puliafito, and J. G. Fujimoto, "Optical Coherence Tomography," Science **254**, 1178-1181 (1991).

38.   "Optical Coherence Tomography - Technology, Markets, and Applications: 2008-2012," BioOptics World (2008).

39.   M. R. Hee, J. A. Izatt, E. A. Swanson, D. Huang, J. S. Schuman, C. P. Lin, C. A. Puliafito, and J. G. Fujimoto, "Optical Coherence Tomography of the Human Retina," Archives of Ophthalmology **113**, 325-332 (1995).

40.   C. A. Puliafito, M. R. Hee, C. P. Lin, E. Reichel, J. S. Schuman, J. S. Duker, J. A. Izatt, E. A. Swanson, and J. G. Fujimoto, "Imaging of Macular Diseases with Optical Coherence Tomography," Ophthalmology **102**, 217-229 (1995).

41.   M. R. Hee, C. R. Baumal, C. A. Puliafito, J. S. Duker, E. Reichel, J. R. Wilkins, J. G. Coker, J. S. Schuman, E. A. Swanson, and J. G. Fujimoto, "Optical coherence tomography of age-related macular degeneration and choroidal neovascularization," Ophthalmology **103**, 1260-1270 (1996).

42.   E. Z. Blumenthal, J. M. Williams, R. N. Weinreb, C. A. Girkin, C. C. Berry, and L. M. Zangwill, "Reproducibility of nerve fiber layer thickness measurements by use of optical coherence tomography," Ophthalmology **107**, 2278-2282 (2000).

43.   M. Wojtkowski, R. Leitgeb, A. Kowalczyk, T. Bajraszewski, and A. F. Fercher, "In vivo human retinal imaging by Fourier domain optical coherence tomography," Journal of Biomedical Optics **7**, 457-463 (2002).

44.   N. A. Nassif, B. Cense, B. H. Park, M. C. Pierce, S. H. Yun, B. E. Bouma, G. J. Tearney, T. C. Chen, and J. F. de Boer, "In vivo high-resolution video-rate spectral-domain optical coherence tomography of the human retina and optic nerve," Optics Express **12**, 367-376 (2004).

45.   M. E. Brezinski, G. J. Tearney, N. J. Weissman, S. A. Boppart, B. E. Bouma, M. R. Hee, A. E. Weyman, E. A. Swanson, J. F. Southern, and J. G. Fujimoto, "Assessing atherosclerotic plaque morphology: Comparison of optical coherence tomography and high frequency intravascular ultrasound," Heart **77**, 397-403 (1997).

46.   I. K. Jang, G. J. Tearney, B. MacNeill, M. Takano, F. Moselewski, N. Iftima, M. Shishkov, S. Houser, H. T. Aretz, E. F. Halpern, and B. E. Bouma, "In vivo characterization of coronary atherosclerotic plaque by use of optical coherence tomography," Circulation **111**, 1551-1555 (2005).

47.   B. E. Bouma, G. J. Tearney, C. C. Compton, and N. S. Nishioka, "Endoscopic optical coherence tomography of the gastrointestinal tract," Gastrointestinal Endoscopy **49**, Ab152-Ab152 (1999).

48.   S. Brand, J. M. Poneros, B. E. Bouma, G. J. Tearney, C. C. Compton, and N. S. Nishioka, "Optical coherence tomography in the gastrointestinal tract," Endoscopy **32**, 796-803 (2000).

49.   M. V. Sivak, K. Kobayashi, J. A. Izatt, A. M. Rollins, R. Ung-runyawee, A. Chak, R. C. K. Wong, G. A. Isenberg, and J. Willis, "High-resolution endoscopic imaging of the GI tract using optical coherence tomography," Gastrointestinal Endoscopy **51**, 474-479 (2000).

50.   J. Welzel, "Optical coherence tomography in dermatology: a review," Skin Research and Technology **7**, 1-9 (2001).

93

51.   M. C. Pierce, J. Strasswimmer, B. H. Park, B. Cense, and J. F. de Boer, "Advances in optical coherence tomography imaging for dermatology," Journal of Investigative Dermatology **123**, 458-463 (2004).

52.   S. A. Boppart, "Optical coherence tomography: Technology and applications for neuroimaging," Psychophysiology **40**, 529-541 (2003).

53.   M. Lazebnik, D. L. Marks, K. Potgieter, R. Gillette, and S. A. Boppart, "Functional optical coherence tomography for detecting neural activity through scattering changes," Optics Letters **28**, 1218-1220 (2003).

54.   B. W. Colston, U. S. Sathyam, L. B. DaSilva, M. J. Everett, P. Stroeve, and L. L. Otis, "Dental OCT," Optics Express **3**, 230-238 (1998).

55.   X. J. Wang, T. E. Milner, J. F. de Boer, Y. Zhang, D. H. Pashley, and J. S. Nelson, "Characterization of dentin and enamel by use of optical coherence tomography," Applied Optics **38**, 2092-2096 (1999).

56.   S. A. Boppart, M. E. Brezinski, B. E. Bouma, G. J. Tearney, and J. G. Fujimoto, "Investigation of developing embryonic morphology using optical coherence tomography," Developmental Biology **177**, 54-63 (1996).

57.   S. A. Boppart, G. J. Tearney, B. E. Bouma, J. F. Southern, M. E. Brezinski, and J. G. Fujimoto, "Noninvasive assessment of the developing Xenopus cardiovascular system using optical coherence tomography," Proceedings of the National Academy of Sciences of the United States of America **94**, 4256-4261 (1997).

58.   Z. P. Chen, T. E. Milner, D. Dave, and J. S. Nelson, "Optical Doppler tomographic imaging of fluid flow velocity in highly scattering media," Optics Letters **22**, 64-66 (1997).

59.   Z. P. Chen, T. E. Milner, S. Srinivas, X. J. Wang, A. Malekafzali, M. J. C. vanGemert, and J. S. Nelson, "Noninvasive imaging of in vivo blood flow velocity using optical Doppler tomography," Optics Letters **22**, 1119-1121 (1997).

60.   J. A. Izatt, M. D. Kulkami, S. Yazdanfar, J. K. Barton, and A. J. Welch, "In vivo bidirectional color Doppler flow imaging of picoliter blood volumes using optical coherence tomograghy," Optics Letters **22**, 1439-1441 (1997).

61.   M. D. Kulkarni, T. G. van Leeuwen, S. Yazdanfar, and J. A. Izatt, "Velocity-estimation accuracy and frame-rate limitations in color Doppler optical coherence tomography," Optics Letters **23**, 1057-1059 (1998).

62.   Y. H. Zhao, Z. P. Chen, C. Saxer, S. H. Xiang, J. F. de Boer, and J. S. Nelson, "Phase-resolved optical coherence tomography and optical Doppler tomography for imaging blood flow in human skin with fast scanning speed and high velocity sensitivity," Optics Letters **25**, 114-116 (2000).

63. L. Li, K. Maslov, G. Ku, and L. V. Wang, "Three-dimensional combined photoacoustic and optical coherence microscopy for in vivo microcirculation studies," Optics Express **17**, 16450-16455 (2009).

64. International Human Genome Sequencing Consortium, "Finishing the euchromatic sequence of the human genome," Nature **431**, 931-945 (2004).

65. F. S. Collins, E. D. Green, A. E. Guttmacher, and M. S. Guyer, "A vision for the future of genomics research," Nature **422**, 835-847 (2003).

66. "Gene expression," http://en.wikipedia.org/wiki/Gene_expression, Accessed Oct. 21, 2010.

67. Y. Taniguchi, P. J. Choi, G. W. Li, H. Y. Chen, M. Babu, J. Hearn, A. Emili, and X. S. Xie, "Quantifying E-coli Proteome and Transcriptome with Single-Molecule Sensitivity in Single Cells," Science **329**, 533-538 (2010).

68. R. Weissleder, and U. Mahmood, "Molecular imaging," Radiology **219**, 316-333 (2001).

69. T. F. Massoud, and S. S. Gambhir, "Molecular imaging in living subjects: seeing fundamental biological processes in a new light," Genes & Development **17**, 545-580 (2003).

70. H. R. Herschman, "Molecular imaging: Looking at problems, seeing solutions," Science **302**, 605-608 (2003).

71. S. S. Gambhir, J. Czernin, J. Schwimmer, D. H. S. Silverman, R. E. Coleman, and M. E. Phelps, "A tabulated summary of the FDG PET literature," Journal of Nuclear Medicine **42**, 1S-93S (2001).

72. R. Weissleder, and M. J. Pittet, "Imaging in the era of molecular oncology," Nature **452**, 580-589 (2008).

73. H. R. Herschman, "Noninvasive imaging of reporter gene expression in living subjects," Advances in Cancer Research, **92**, 29-80 (2004).

74. P. Ray, H. Pimenta, R. Paulmurugan, F. Berger, M. E. Phelps, M. Iyer, and S. S. Gambhir, "Noninvasive quantitative imaging of protein-protein interactions in living subjects," Proceedings of the National Academy of Sciences of the United States of America **99**, 3105-3110 (2002).

75. L. A. Green, C. S. Yap, K. Nguyen, J. R. Barrio, M. Namavari, N. Satyamurthy, M. E. Phelps, E. P. Sandgren, H. R. Herschman, and S. S. Gambhir, "Indirect monitoring of endogenous gene expression by positron emission tomography (PET) imaging of reporter gene expression in transgenic mice," Molecular Imaging & Biology **4**, 71-81 (2002).

76.   I. Serganova, V. Ponomarev, and R. Blasberg, "Human reporter genes: potential use in clinical studies," Nuclear Medicine and Biology **34**, 791-807 (2007).

77.   S. S. Gambhir, "Molecular imaging of cancer with positron emission tomography," Nature Reviews Cancer **2**, 683-693 (2002).

78.   K. M. Brindle, "Molecular imaging using magnetic resonance: new tools for the development of tumour therapy," British Journal of Radiology **76**, S111-S117 (2003).

79.   Y. W. Wang, X. Y. Xie, X. D. Wang, G. Ku, K. L. Gill, D. P. O'Neal, G. Stoica, and L. V. Wang, "Photoacoustic tomography of a nanoshell contrast agent in the in vivo rat brain," Nano Letters **4**, 1689-1692 (2004).

80.   D. Razansky, C. Vinegoni, and V. Ntziachristos, "Multispectral photoacoustic imaging of fluorochromes in small animals," Optics Letters **32**, 2891-2893 (2007).

81.   A. De La Zerda, C. Zavaleta, S. Keren, S. Vaithilingam, S. Bodapati, Z. Liu, J. Levi, B. R. Smith, T. J. Ma, O. Oralkan, Z. Cheng, X. Y. Chen, H. J. Dai, B. T. Khuri-Yakub, and S. S. Gambhir, "Carbon nanotubes as photoacoustic molecular imaging agents in living mice," Nature Nanotechnology **3**, 557-562 (2008).

82.   C. Kim, E. C. Cho, J. Y. Chen, K. H. Song, L. Au, C. Favazza, Q. A. Zhang, C. M. Cobley, F. Gao, Y. N. Xia, and L. H. V. Wang, "In vivo molecular Photoacoustic Tomography of Melanomas Targeted by Bioconjugated Gold Nanocages," Acs Nano **4**, 4559-4564 (2010).

83.   D. Razansky, M. Distel, C. Vinegoni, R. Ma, N. Perrimon, R. W. Koster, and V. Ntziachristos, "Multispectral opto-acoustic tomography of deep-seated fluorescent proteins in vivo," Nature Photonics **3**, 412-417 (2009).

84.   R. Weissleder, A. Moore, U. Mahmood, R. Bhorade, H. Benveniste, E. A. Chiocca, and J. P. Basilion, "In vivo magnetic resonance imaging of transgene expression," Nature Medicine **6**, 351-355 (2000).

85.   T. Groot-Wassink, E. O. Aboagye, Y. H. Wang, N. R. Lemoine, A. J. Reader, and G. Vassaux, "Quantitative imaging of Na/I symporter transgene expression using positron emission tomography in the living animal," Molecular Therapy **9**, 436-442 (2004).

86.   P. R. Contag, I. N. Olomu, D. K. Stevenson, and C. H. Contag, "Bioluminescent indicators in living mammals," Nature Medicine **4**, 245-247 (1998).

87.   M. Chalfie, Y. Tu, G. Euskirchen, W. W. Ward, and D. C. Prasher, "Green fluorescent protein as a aarker for gene-expression," Science **263**, 802-805 (1994).

88.   C. Cepko, E. Ryder, D. M. Fekete, and S. Bruhn, "Detection of beta-galactosidase and alkaline phosphatase activities in tissue," in *Cells: A Laboratory Manual, Volume 3: Subcellular Location of Genes and Their Products*, D. L. Spector, R. D. Goldman, and L. A. Leinwand, eds. (Cold Spring Harbor Laboratory Press, Cold Spring Harbor 1998).

89.   J. R. Sanes, J. L. R. Rubenstein, and J. F. Nicolas, "Use of a Recombinant Retrovirus to Study Postimplantation Cell Lineage in Mouse Embryos," Embo Journal **5**, 3133-3142 (1986).

90.   P. M. Ismail, J. Li, F. J. DeMayo, B. W. O'Malley, and J. P. Lydon, "A novel lacZ reporter mouse reveals complex regulation of the progesterone receptor promoter during mammary gland development," Molecular Endocrinology **16**, 2475-2489 (2002).

91.   W. C. Lin, T. P. Pretlow, T. G. Pretlow, and L. A. Culp, "Bacterial lacZ Gene as a Highly Sensitive Marker to Detect Micrometastasis Formation during Tumor Progression," Cancer Research **50**, 2808-2817 (1990).

92.   L. A. Lampson, M. A. Lampson, and A. D. Dunne, "Exploiting the lacZ Reporter Gene for Quantitative-Analysis of Disseminated Tumor-Growth within the Brain - Use of the lacZ Gene-Product as a Tumor-Antigen, for Evaluation of Antigenic Modulation, and to Facilitate Image-Analysis of Tumor-Growth Insitu," Cancer Research **53**, 176-182 (1993).

93.   H. D. Nickerson, and W. H. Colledge, "A lacZ-based transgenic mouse for detection of somatic gene repair events in vivo," Gene Therapy **11**, 1351-1357 (2004).

94.   A. Y. Louie, M. M. Huber, E. T. Ahrens, U. Rothbacher, R. Moats, R. E. Jacobs, S. E. Fraser, and T. J. Meade, "In vivo visualization of gene expression using magnetic resonance imaging," Nature Biotechnology **18**, 321-325 (2000).

95.   C. H. Tung, Q. Zeng, K. Shah, D. E. Kim, D. Schellingerhout, and R. Weissleder, "In vivo imaging of beta-galactosidase activity using far red fluorescent switch," Cancer Research **64**, 1579-1583 (2004).

96.   P. Okunieff, J. Williams, Y. Chen, S. Nioka, S. Wen, J. Zhang, J. Du, X. Intes, Z. Zhao, and B. Chance, "Simulation Study of Breast Tissue Hemodynamics During Pressure Perturbation," in *Oxygen Transport to Tissue XXVI*(Springer US, 2005), pp. 17-22.

97.   M. Xu, and L. V. Wang, "Universal back-projection algorithm for photoacoustic computed tomography," Physical Review E **71**, 016706 (2005).

98.   C. Kim, T. N. Erpelding, L. Jankovic, M. D. Pashley, and L. V. Wang, "Deeply penetrating in vivo photoacoustic imaging using a clinical ultrasound array system," Biomedical Optics Express **1**, 278-284 (2010).

99.   K. P. Köstli, M. Frenz, H. Bebie, and H. P. Weber, "Temporal backward projection of optoacoustic pressure transients using Fourier transform methods," Physics in Medicine and Biology **46**, 1863 (2001).

100.   M. Li, H. F. Zhang, K. Maslov, G. Stoica, and L. V. Wang, "Improved in vivo photoacoustic microscopy based on a virtual-detector concept," Optics Letters **31**, 474-476 (2006).

101. C. Zhang, K. Maslov, and L. V. Wang, "Subwavelength-resolution label-free photoacoustic microscopy of optical absorption in vivo," Opt. Lett. **35**, 3195-3197 (2010).

102. B. Fargell, and M. Intaglietta, "Microcirculation: its significance in clinical and molecular medicine," Journal of Internal Medicine **241**, 349-362 (1997).

103. R. K. Jain, L. L. Munn, and D. Fukumura, "Dissecting tumour pathophysiology using intravital microscopy," Nature Reviews Cancer **2**, 266-276 (2002).

104. W. Groner, J. W. Winkelman, A. G. Harris, C. Ince, G. J. Bouma, K. Messmer, and R. G. Nadeau, "Orthogonal polarization spectral imaging: A new method for study of the microcirculation," Nature Medicine **5**, 1209-1213 (1999).

105. J. Seylaz, R. Charbonne, K. Nanri, D. Von Euw, J. Borredon, K. Kacem, P. Meric, and E. Pinard, "Dynamic in vivo measurement of erythrocyte velocity and flow in capillaries and of microvessel diameter in the rat brain by confocal laser microscopy," Journal of Cerebral Blood Flow and Metabolism **19**, 863-870 (1999).

106. E. B. Brown, R. B. Campbell, Y. Tsuzuki, L. Xu, P. Carmeliet, D. Fukumura, and R. K. Jain, "In vivo measurement of gene expression, angiogenesis and physiological function in tumors using multiphoton laser scanning microscopy," Nature Medicine **7**, 864-868 (2001).

107. E. Eriksson, J. V. Boykin, and R. N. Pittman, "Method for in vivo microscopy of the cutaneous microcirculation of the hairless mouse ear," Microvascular Research **19**, 374-379 (1980).

108. L. A. Holowatz, C. S. Thompson-Torgerson, and W. L. Kenney, "The human cutaneous circulation as a model of generalized microvascular function," Journal of Applied Physiology **105**, 370-372 (2008).

109. I. M. Braverman, "The cutaneous microcirculation," Journal of Investigative Dermatology Symposium Proceedings **5**, 3-9 (2000).

110. R. Brancato, F. Bandello, and R. Lattanzio, "Iris fluorescein angiography in clinical practice," Survey of Ophthalmology **42**, 41-70 (1997).

111. R. Langer, and J. P. Vacanti, "Tissue engineering," Science **260**, 920-926 (1993).

112. L. G. Griffith, and G. Naughton, "Tissue Engineering--Current Challenges and Expanding Opportunities," Science **295**, 1009-1014 (2002).

113. S.-W. Choi, J. Xie, and Y. Xia, "Chitosan-Based Inverse Opals: Three-Dimensional Scaffolds with Uniform Pore Structures for Cell Culture," Advanced Materials **21**, 2997-3001 (2009).

114.   G. Yao, and L. H. V. Wang, "Monte Carlo simulation of an optical coherence tomography signal in homogeneous turbid media," Physics in Medicine and Biology **44**, 2307-2320 (1999).

115.   L. V. Wang, S. L. Jacques, and L. Zheng, "MCML--Monte Carlo modeling of light transport in multi-layered tissues," Computer Methods and Programs in Biomedicine **47**, 131-146 (1995).

116.   U. Morgner, W. Drexler, F. X. Kartner, X. D. Li, C. Pitris, E. P. Ippen, and J. G. Fujimoto, "Spectroscopic optical coherence tomography," Optics Letters **25**, 111-113 (2000).

117.   A. Dunn, and D. Boas, "Transport-based image reconstruction in turbid media with small source-detector separations," Optics Letters **25**, 1777-1779 (2000).

118.   E. M. C. Hillman, D. A. Boas, A. M. Dale, and A. K. Dunn, "Laminar optical tomography: demonstration of millimeter-scale depth-resolved imaging in turbid media," Optics Letters **29**, 1650-1652 (2004).

119.   J. C. Hebden, and D. T. Delpy, "Enhanced Time-Resolved Imaging with a Diffusion-Model of Photon Transport," Optics Letters **19**, 311-313 (1994).

120.   F. E. W. Schmidt, M. E. Fry, E. M. C. Hillman, J. C. Hebden, and D. T. Delpy, "A 32-channel time-resolved instrument for medical optical tomography," Review of Scientific Instruments **71**, 256-265 (2000).

121.   C. D'Andrea, D. Comelli, A. Pifferi, A. Torricelli, G. Valentini, and R. Cubeddu, "Time-resolved optical imaging through turbid media using a fast data acquisition system based on a gated CCD camera," Journal of Physics D-Applied Physics **36**, 1675-1681 (2003).

122.   S. C. Mishra, P. Chugh, P. Kumar, and K. Mitra, "Development and comparison of the DTM, the DOM and the FVM formulations for the short-pulse laser transport through a participating medium," International Journal of Heat and Mass Transfer **49**, 1820-1832 (2006).

123.   M. R. Hee, J. A. Izatt, E. A. Swanson, and J. G. Fujimoto, "Femtosecond transillumination tomography in thick tissues," Opt. Lett. **18**, 1107-1109 (1993).

124.   J. C. Dainty, *Laser speckle and related phenomena* (Springer-Verlag Berlin and New York, 1975).

125.   J. W. Goodman, *Speckle phenomena in optics: Theory and applications* (Roberts & Company, Englewood, 2007).

126.   C. B. Burckhardt, "Speckle in ultrasound B-mode scans," IEEE Transactions on Sonics and Ultrasonics **25**, 1-6 (1978).

127.   R. F. Wagner, S. W. Smith, J. M. Sandrik, and H. Lopez, "Statistics of Speckle in Ultrasound B-Scans," IEEE Transactions on Sonics and Ultrasonics **30**, 156-163 (1983).

128.   J. S. Lee, "Speckle suppression and analysis for synthetic aperture radar images," Opt. Eng. **25**, 636-643 (1986).

129.   J. M. Schmitt, S. H. Xiang, and K. M. Yung, "Speckle in Optical Coherence Tomography," Journal of Biomedical Optics **4**, 95-105 (1999).

130.   G. J. Diebold, T. Sun, and M. I. Khan, "Photoacoustic monopole radiation in one, two, and three dimensions," Physical Review Letters **67**, 3384 (1991).

131.   P. M. Morse, and K. U. Ingard, *Theoretical Acoustics* (McGraw-Hill, New York, 1968).

132.   K. K. Shung, and G. A. Thieme, *Ultrasound Scattering in Biological Tissues* (CRC Press, Florida, 1993).

133.   J. A. Jensen, and N. B. Svendsen, "Calculation of pressure fields from arbitrarily shaped, apodized, and excited ultrasound transducers," IEEE Transactions on Ultrasonics, Ferroelectrics and Frequency Control **39**, 262-267 (1992).

134.   J. A. Jensen, and N. B. Svendsen, "Calculation of pressure fields from arbitrarily shaped, apodized, and excited ultrasound transducers," IEEE Transactions on Ultrasonics, Ferroelectrics and Frequency Control, **39**, 262-267 (1992).

135.   V. L. Newhouse, and I. Amir, "Estimation of scatterer volume density near a concentration gradient," Ultrasonic Imaging **7**, 161-171 (1985).

Vita

Li Li

Date of Birth   Jun. 4, 1981

Place of Birth   Jingjiang, Jiangsu, People's Republic of China

Degrees   B.Sc. in Biomedical Engineering, 2003.

Ph.D. in Biomedical Engineering, 2010.

Publications   [B. Rao*, <u>L. Li</u>*], K. Maslov, and L. V. Wang, "Hybrid-scanning optical-resolution photoacoustic microscopy system for in vivo vasculature imaging," *Optics Letters* 35, 1521–1523 (2010) (*The Authors contributed equally to this work.)

G. Ku, K. Maslov, L. Li, and L. V. Wang, "Photoacoustic microscopy with 2-µm transverse resolution," *Journal of Biomedical Optics (Letters)* 15, 021302 (2010).

<u>L. Li</u>, K. Maslov, G. Ku, and L. V. Wang, "Three-dimensional combined photoacoustic and optical coherence microscopy for in vivo microcirculation studies," *Optics Express* 17, 16450–16455 (2009).

[Z. Guo*, <u>L. Li</u>*], and L. V. Wang, "On the speckle-free nature of photoacoustic tomography," *Medical Physics* 36, 4084–4088 (2009).

(*The Authors contributed equally to this work.)

L. Li, H. F. Zhang, R. J. Zemp, K. Maslov, and L. V. Wang, "Simultaneous imaging of a lacZ-marked tumor and microvasculature morphology in vivo by dual-wavelength photoacoustic microscopy," *Journal of Innovative Optical Health Sciences* 1, 207–215 (2008).

L. Li, and L. V. Wang, "Optical coherence computed tomography," *Applied Physics Letters* 91, 141107 (2007).

[L. Li*, R. Zemp], G. Lungu, G. Stoica, and L. V. Wang, "Photoacoustic imaging of lacZ gene expression in vivo," *Journal of Biomedical Optics (Letters)* 12, 020504 (2007). (*The Authors contributed equally to this work.)

Dec. 2010